ULK4 and Fused/STK36 interact to mediate assembly of a motile flagellum

Ciaran J. McCoy[a,†], Humbeline Paupelin-Vaucelle[a], Peter Gorilak[b], Tom Beneke[a], Vladimir Varga[b], and Eva Gluenz[a,c,‡,*]

[a]Sir William Dunn School of Pathology, University of Oxford, Oxford OX1 3RE, United Kingdom; [b]Institute of Molecular Genetics of the Czech Academy of Sciences, Prague, 142 20 Prague 4, Czech Republic; [c]Wellcome Centre for Integrative Parasitology, School of Infection and Immunity, University of Glasgow, Glasgow G12 8TA, United Kingdom

ABSTRACT **Unc-51–like kinase (ULK) family serine–threonine protein kinase homologues have been linked to the function of motile cilia in diverse species. Mutations in Fused/STK36 and ULK4 in mice resulted in hydrocephalus and other phenotypes consistent with ciliary defects. How either protein contributes to the assembly and function of motile cilia is not well understood. Here we studied the phenotypes of *ULK4* and *Fused* gene knockout (KO) mutants in the flagellated protist *Leishmania mexicana*. Both KO mutants exhibited a variety of structural defects of the flagellum cytoskeleton. Biochemical approaches indicate spatial proximity of these proteins and indicate a direct interaction between the N-terminus of LmxULK4 and LmxFused. Both proteins display a dispersed localization throughout the cell body and flagellum, with enrichment near the flagellar base and tip. The stable expression of LmxULK4 was dependent on the presence of LmxFused. Fused/STK36 was previously shown to localize to mammalian motile cilia, and we demonstrate here that ULK4 also localizes to the motile cilia in mouse ependymal cells. Taken together these data suggest a model where the pseudokinase ULK4 is a positive regulator of the kinase Fused/ STK36 in a pathway required for stable assembly of motile cilia.**

Monitoring Editor
Gregory Pazour
University of Massachusetts Medical School

Received: Aug 15, 2022
Revised: Mar 10, 2023
Accepted: Mar 21, 2023

INTRODUCTION

Serine–threonine protein kinases of the Unc-51–like kinase (ULK) family are found across eukaryotic species, with the best-characterized members found in metazoans and plants. In mammals the family has four active kinases (ULK1, ULK2, ULK3, and Fused/STK36) and one pseudokinase (ULK4). The active kinases function in multiple well-studied biological processes: ULK1 and ULK2 act in autophagy pathways in starvation responses (Lee, 2011), ULK3 is a regulator of the sonic hedgehog signaling pathway (Maloverjan *et al.*, 2010), and Fused kinase was first identified in *Drosophila* (Preat *et al.*, 1990) as a kinase of the Hedgehog (Hh) signaling pathway. Unexpectedly, studies on the mouse Fused homologue, also named Serine/threonine-protein kinase 36 (STK36), showed that *Fused* knockout (KO) mice did not show any defects in Hh signaling (Chen *et al.*, 2005; Merchant *et al.*, 2005). Instead, it was found that these mice developed hydrocephalus and respiratory infections and died a few weeks after birth (Merchant *et al.*, 2005). This phenotype, together with the finding that Fused was highly expressed in ependymal cells and nasal epithelium, pointed to a function in cells with motile cilia.

Cilia and flagella are cellular appendages formed by a microtubule axoneme that originates at the basal body and has more or less extensive structural elaborations, depending on its specific function within a cell type. A key distinction is between motile cilia/flagella, which typically have a so-called 9+2 axoneme composed of a pair of singlet microtubules (central pair; CP) surrounded by a ring of nine doublet microtubules. The latter are decorated with axonemal dyneins and other protein complexes such as radial spokes (RSP)

This article was published online ahead of print in MBoC in Press (http://www.molbiolcell.org/cgi/doi/10.1091/mbc.E22-06-0222) on March 29, 2023.

Conflict of interest: No competing interests declared.

Present address: †Microbes & Pathogen Biology, The Institute for Global Food Security, School of Biological Sciences, Queen's University Belfast, Belfast BT9 5DL, United Kingdom; ‡Institute of Cell Biology, Baltzerstrasse 4, University of Bern, 3012 Bern, Switzerland.

*Address correspondence to: Eva Gluenz (eva.gluenz@unibe.ch).

Abbreviations used: BioID, proximity-dependent protein identification; FAZ, flagellar attachment zone; Hh, Hedgehog; IFT, intraflagellar transport; IP, immunoprecipitation; KO, knockout; mNG, mNeonGreen; PBS, phosphate buffered saline; PKD, primary ciliary dyskinesia; RNAi, RNA interference; RSP, radial spokes; TEM, transmission electron microscopy; ULK, Unc-51-like kinase.

required for bending. They provide one of the main modes of eukaryotic cell motility, as used by many protists, unicellular plants, and gametes of diverse species including mammalian sperm cells. Cells extending motile cilia are also found within tissues where they generate directional fluid flow required for development and normal physiology (Ringers *et al.*, 2020), for example, ciliated ependymal cells of the brain ventricles and spinal canal help the circulation of cerebrospinal fluid. Primary cilia by contrast have a simpler axoneme structure consisting of nine doublet microtubules, and they transduce chemical and mechanical signals from the environment (Goetz and Anderson, 2010). Cilia and flagella construction relies on a conserved intraflagellar transport (IFT) system that shuttles cargo, including axonemal constituents, from the basal body to the axoneme tip and back (Lechtreck, 2015).

Wilson *et al.* (2009) investigated whether mammalian Fused was required for the Hh responses mediated through primary cilia and found that this was not the case: *Fu*$^{-/-}$ mice were capable of constructing normal primary cilia. By contrast, *Fu*$^{-/-}$ mice had motile cilia defects, with 60% showing an abnormal ultrastructure (40% of cilia had no CP) and misalignment, which resulted in uncoordinated ciliary beating. Unlike the situation in mice, morpholino-mediated knockdown of *Fu* in zebrafish did affect Hh signaling, and in addition, the morphants also had structurally and functionally disrupted cilia in Kupffer's vesicle that are required in development to generate a directional fluid flow to establish the body's left–right axis. The effect on the cilia was independent of Hh signaling, indicating that this kinase acts in multiple conserved pathways in different lineages (Wilson *et al.*, 2009). Studies on oviduct cilia provided further evidence for an important role of mammalian Fused/STK36 in motile cilia. The majority of oviduct cilia in *Fu*$^{-/-}$ mice had an abnormal axoneme structure (Nozawa *et al.*, 2013): cilia were misaligned, and a majority of these oviduct cilia lacked CP microtubules within tissues that also produced some cilia with a normal 9+2 architecture. Mouse sperm flagella function was also affected by conditional deletion of *Fu*, showing motility defects associated with infertility (Nozawa *et al.*, 2014). In the sperm cells the 9+2 microtubule structure of the axoneme was maintained, but they exhibited a defect in the structure of the manchette, a transient microtubule structure required for correct shaping of the sperm head.

In humans, primary ciliary dyskinesia (PCD) is a disease caused by defects in motile cilia that can result from various genetic causes. Fused/STK36 loss-of-function mutations were found in a PCD patient (Edelbusch *et al.*, 2017), where most motile cilia were normal but ~5% had abnormal microtubule numbers and cilia misorientation affected their movement. The Fu protein itself was localized along the length of the motile cilium (Nozawa *et al.*, 2013; Edelbusch *et al.*, 2017), consistent with the genetic evidence for a role of Fused/STK36 in motile cilia. One study suggested that it was sited between the radial spoke heads and the CP microtubules (Edelbusch *et al.*, 2017). Biochemical evidence for an interaction between mouse Fu and the CP-associated protein Spag16/PF20 and several other ciliary proteins led to a model where Fu and the kinesin-like protein Kif27 interact to promote CP assembly in motile cilia of mammals (Wilson *et al.*, 2009).

Less functional information is available for the pseudokinase ULK4, but, as for Fused/STK36, there is converging evidence for a function associated with motile cilia. In a mouse KO and phenotyping screen, ULK4 was identified in a cohort of genes for which disruption caused hydrocephalus (Vogel *et al.*, 2012). This gene cohort also included Fused/STK36 and Kif27. In *ULK4* hypomorph mutant mice, in which *ULK4* expression was reduced, ependymal cells had abnormal axonemes and disorganized cilia (Liu *et al.*, 2016). Abnormal structures included 9+0 and other deviations from normal 9+2 microtubule numbers, while some cilia had normal structures. The possibility was raised that ULK4 regulates different processes of ciliogenesis. RNA-seq showed alterations in cilia-related transcripts and indicated that ULK4 regulated Foxj1 transcription factor pathways involved in ciliogenesis (Liu *et al.*, 2016).

The documented links between ULK4 disruption and human diseases prompted the elucidation of the ULK4-ATPγS complex structure and mapping of the molecular "environment" by proximity labeling (Preuss *et al.*, 2020). The proximity interaction network uncovered five kinases, including Fused/STK36, and proteins associated with a range of different functions, among them ciliary and microtubule-associated proteins.

Orthologues of Fused/STK36 and ULK4 are present in the kinetoplastids, a group of flagellated protozoans that are well-studied on grounds of their medical importance as causative agents of neglected parasitic diseases. In *Trypanosoma brucei*, FCP6/TbFused and FCP5/TbULK4 localized to the flagella connector (Varga *et al.*, 2017), a mobile transmembrane structure at the tip of the newly growing flagellum that connects it to the existing flagellum during a defined phase in the growth cycle (Moreira-Leite *et al.*, 2001). Deletion of *LmxFused* and *LmxULK4* in *Leishmania mexicana* in a "kinome"-wide KO screen yielded cells with shorter flagella and reduced motility (Baker *et al.*, 2021). We independently found *LmxULK4* and *LmxFused* in a screen of flagellar protein KO mutants with reduced motility. This single-celled genetically tractable organism offered an opportunity to conduct a detailed analysis of Fused/STK36 and ULK4 null mutant phenotypes and how their loss has an impact on motile flagella. We found that *LmxULK4* and *LmxFused* KOs both present with the same spectrum of morphological defects, affecting the length and ultrastructure of the flagellar axoneme. This indicates a conserved role for Fused/STK36 or ULK4 in ciliogenesis and cilia function. Our data support a model whereby these two proteins directly interact with each other to promote stable assembly of motile flagella in evolutionarily distant lineages. Consistent with this model, we also show that the mammalian ULK4 protein localizes to the motile cilium of mouse ependymal cells.

RESULTS

LmxULK4 and LmxFused localize to both the cell body and motile flagellum of *Leishmania*

LmxULK4 and *LmxFused* encode UNC-51–like proteins that are orthologues of animal ULK4 and Fused/STK36, respectively (Figure 1A). Like its mammalian orthologues, LmxULK4 represents a catalytically inactive pseudokinase, as supported by the lack of the catalytically important lysine residue within the typically highly conserved "VAIK" motif (see Figure 1B). We assessed protein localization by inserting an mNeonGreen (mNG) fusion tag at the endogenous gene locus (tagging both alleles of the gene) and imaging the fusion proteins in live cells. Both proteins localized to the *Leishmania* promastigote cell body and motile flagellum throughout the cell cycle (Figure 1, C–E). Individual cells (both dividing and nondividing) often displayed enriched signal at the flagellum tip, base, or both, but no evidence was found for a dominant signal uniquely localized at the tip of the newly growing flagellum, where the orthologous *T. brucei* proteins are localized (Varga *et al.*, 2017). The LmxFused::mNG and LmxULK4::mNG fluorescent signal was absent in cells extracted with a nonionic detergent (Supplemental Figure 1), suggesting that neither protein is tightly attached to the insoluble cytoskeleton.

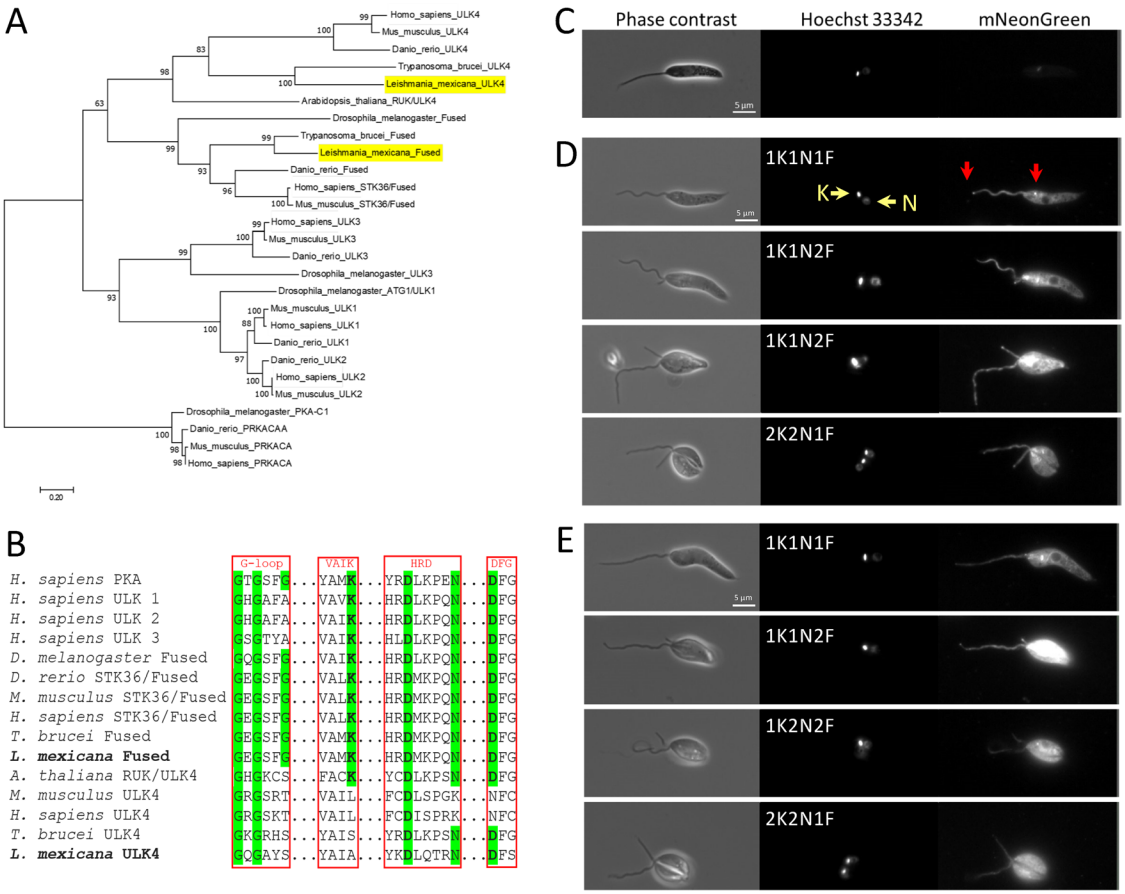

FIGURE 1: UNC-51–like kinase orthologues in *L. mexicana* and their subcellular localization. (A) Position of *L. mexicana* (Lmx) Fused and *Lmx*ULK4 in relation to UNC-51–like kinases. Maximum likelihood tree based on the LG (+*G*+*I*) model of evolution and with 500 bootstrap replicates (MEGA 7; Kumar *et al.*, 2016); sequences used: *Homo sapiens* ULK1 (O75385), ULK2 (Q8IYT8), ULK3 (Q6PHR2), ULK4 (Q96C45), STK36/Fused (Q9NRP7), PRKACA (P17612); *Mus musculus* ULK1 (O70405), ULK2 (Q9QY01), ULK3 (Q3U3Q1), ULK4 (Q3V129), STK36/Fused (Q69ZM6), PRKACA (P05132); *Danio rerio* ULK1 (F1R9T2), ULK2 (X1WEA3), ULK3 (A4IG43), ULK4 (A0A0R4IA69), Fused (A8WFS2), PRKACAA (A3KMS9); *Drosophila melanogaster* ATG1/ULK1 (Q9VU14), ULK3 (Q9VHF6), Fused (P23647), PKA-C1 (P12370); *Arabidopsis thaliana* RUK/ULK4 (F4JY37), with UniProt IDs in brackets (UniProt Consortium, 2021). *T. brucei* FCP5/ULK4 (Tb927.11.8150), FCP6/Fused (Tb927.11.4470); *L. mexicana* ULK4 (LmxM.28.0620), Fused (LmxM.13.0440) with TritrypDB GeneIDs (Amos *et al.*, 2021) in brackets. (B) Kinase motif ("G-loop," "VAIK," "HRD," and "DFG" motifs)-focused multiple sequence alignment. Catalytically relevant amino acid residues are highlighted in green, with the residues that form the canonical catalytic triad also highlighted in bold. (C–E) Fluorescent micrographs of *L. mexicana* promastigote forms, expressing either no fusion protein (parental control) (C), LmxFused::mNG (D), or LmxULK4::mNG (E). The micrographs show different cell cycle stages, as assessed by the number of kinetoplasts (K), nuclei (N), and flagella (F). Nuclear and kinetoplast DNA were labeled with Hoechst 33342. Red arrows point to the base and tip of the flagellum.

Loss of *LmxULK4* or *LmxFused* leads to failure of normal motile flagellum assembly

To analyze loss-of-function phenotypes, CRISPR/Cas9 was used to knock out *LmxULK4* and *LmxFused*, respectively (Supplemental Figure S2). Measurement of swimming speed showed that this was significantly reduced in both KO lines (Figure 2A), relative to parental controls, consistent with the lack of a long flagellum in the majority (~90–95%) of cells in these KO populations ($n \geq 500$; Figure 2, B and D). The visible flagella that were still present in a minority of the KO cells were shorter than those of the parental controls ($n \geq 27$; Figure 2C; one-way analysis of variance [ANOVA] with the Šídák correction for multiple comparisons). Moreover, although these were not completely paralyzed, they did not enable cell propulsion but rather facilitated a small proportion of cells to twitch at the bottom of their culture dish when observed in vitro. Despite these striking changes in morphology, the KO mutants exhibited only a very slight increase in doubling time (Supplemental Figure S3). Importantly, the flagellum-associated phenotypes reported here were completely rescued via reintroduction of the target gene on an episomal add back plasmid for the Δ*LmxFused* cell line and partially rescued for Δ*LmxULK4* (Figure 2, A–C). A dual KO of both genes (Δ*LmxULK4*/Δ*LmxFused*) resulted in flagellar phenotypes that were indistinguishable to either individual Δ*LmxULK4* and Δ*LmxFused* cell line (Figure 2, A–D).

Δ*LmxULK4* and Δ*LmxFused* mutants display a range of structural defects in the flagellum

These data are consistent with a role for *LmxFused* and *LmxULK4* in the assembly of a motile flagellum (Baker *et al.*, 2021). A striking feature of the KO phenotypes was that within clonal populations of

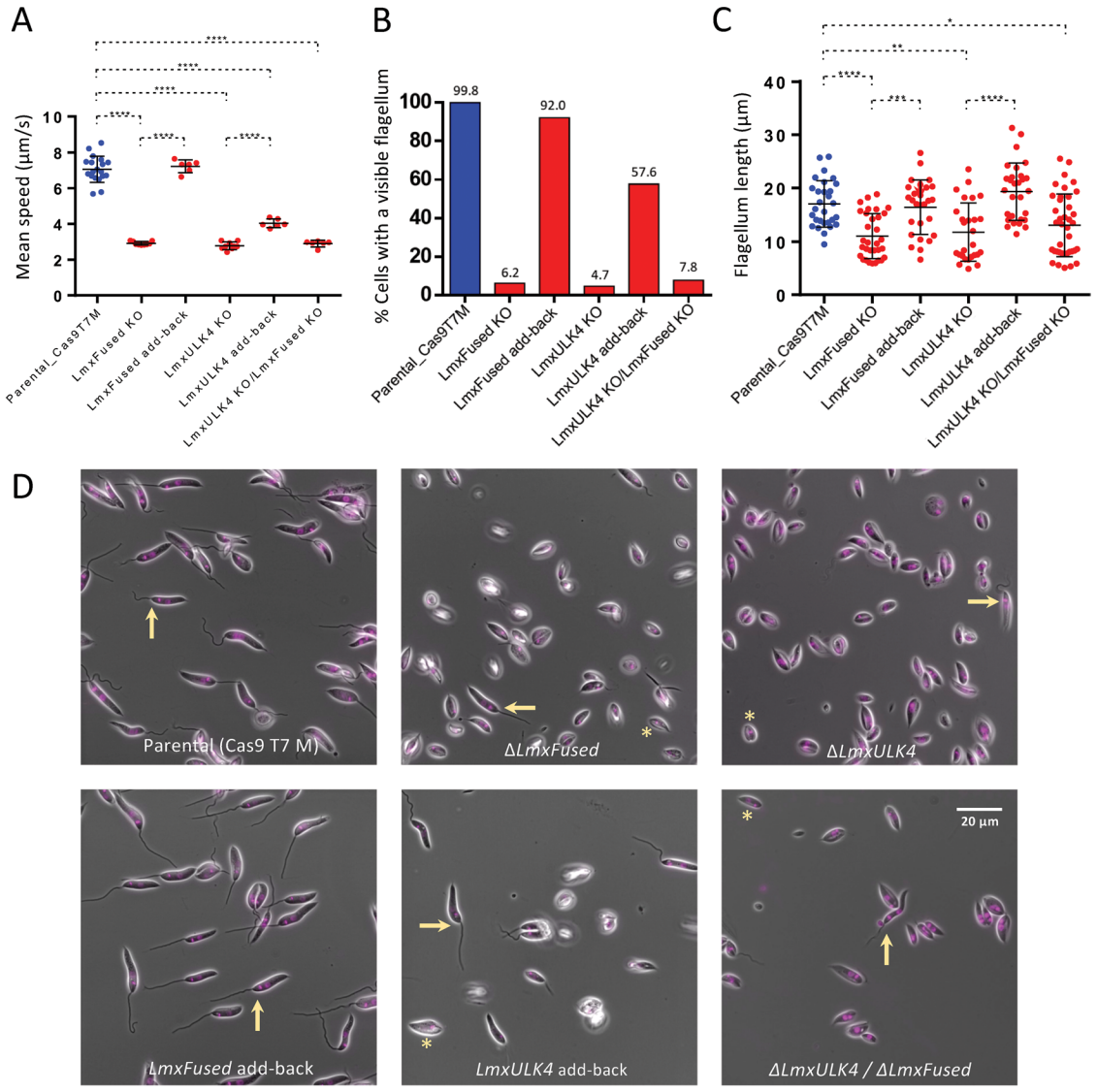

FIGURE 2: Deletion of *LmxULK4* and *LmxFused* results in loss of motile flagella. (A) Swimming speed of the parental *L. mexicana* promastigote cells, *LmxULK4* and *LmxFused* KO mutants, and respective add back cell lines. Three motility assays were performed per promastigote culture analyzed on a given day as standard. Each dot represents the average speed of a population of promastigotes from one motility assay (ordinary one-way ANOVA with Šidák correction for multiple comparisons [$****P \leq 0.0001$; mean ± SD]; Cas9T7M [$n = 19$]; *LmxFused* KO [$n = 9$]; *LmxFused* add back [$n = 6$]; *LmxULK4* KO [$n = 9$]; *LmxULK4* add back [$n = 6$]; *LmxULK4* KO/*LmxFused* KO [$n = 6$]). (B) Proportion of cells with a visible external flagellum (500 individual cells counted per cell line; each cell line was analyzed once). (C) Measurement of flagellar length for cells that had an external flagellum. Each dot represents an individual cell (ordinary one-way ANOVA with Šidák correction for multiple comparisons [$*P \leq 0.05$; $**P \leq 0.01$; $***P \leq 0.001$; $****P \leq 0.0001$; mean ± SD]; Cas9T7M [$n = 29$]; *LmxFused* KO [$n = 32$]; *LmxFused* add back [$n = 27$]; *LmxULK4* KO [$n = 27$]; *LmxULK4* add back [$n = 29$]; *LmxULK4* KO/*LmxFused* KO [$n = 39$]; each cell line was analyzed once). (D) Morphology of the parental cell line, *LmxULK4* and *LmxFused* KOs, and episomal add back cell lines. Images are composites of the phase-contrast channel and a fluorescence channel showing nuclear and kinetoplast DNA labeled with Hoechst 33342. Arrows point to examples of cells with a visible external flagellum. An asterisk highlights example cells that lack a visible external flagellum.

apparently aflagellate cells, a small but stable proportion of cells did still possess a long flagellum. This suggests that LmxULK4 or LmxFused is not strictly essential for the formation of a flagellum but their absence prevented the reliable assembly of functional motile flagella in most cells. To understand which step of flagellum biogenesis failed in these mutants, the structure of the remaining flagella in the Δ*LmxFused* and Δ*LmxULK4* populations was examined in detail. The axonemal radial spoke protein 11 (RSP11; LmxM.09.1530) and the CP-associated protein PF16 (LmxM.20.1400) were chosen as reporter proteins for key structures of the motile axoneme, and a cell line was generated simultaneously expressing RSP11::eYFP and PF16::mStrawberry (Pf16::mStr) fluorescent fusion proteins. In this cell line, *LmxFused* and *LmxULK4* were then deleted, respectively (Figure 3, A and B). This showed that Δ*LmxFused* and Δ*LmxULK4* exhibit highly similar proportions of multiple distinct flagellar morphotypes and effectively phenocopy each other (Figure 3B). In both

KO cell lines, ~2/3 of cells not only lacked a long external flagellum (as observed in the untagged cell lines [Figure 2, B and D]), but the absence of RSP11::eYFP and PF16::mStr fluorescent signals at the anterior cell pole, where the flagellum normally emerges from the flagellar pocket, indicated that these cells lacked axonemes entirely (Figure 3Bv).

Defects in the CP were previously reported for distinct ciliated tissues in both ULK4 and Fused/STK36 mutant mice (Wilson *et al.*, 2009; Nozawa *et al.*, 2013; Liu *et al.*, 2016). Moreover, the CP microtubule-associated protein PF20 (but not PF16) has previously been shown to coimmunoprecipitate with Fused/STK36 when expressed in HEK 293T cells (Wilson *et al.*, 2009). Examination of PF16::mStr signals (Figure 3, A and B) found that a majority of cells with a long flagellum still possessed a continuous PF16 signal (Figure 3B), suggesting that the CP was still assembled in these cells, and a disrupted signal was observed in only a small percentage of flagella. To examine whether PF20 was affected by the loss of *LmxFused* and *LmxULK4*, each gene was deleted in a reporter cell line expressing PF16::eYFP/mStr::PF20 (Figure 3, C and D). Focusing on the external flagella that still showed a continuous PF16::eYFP signal, we measured the intensity of fluorescence and detected a reduced signal intensity for mStr::PF20 in both Δ*LmxFused* and Δ*LmxULK4* cell lines, while no reduction of the PF16::eYFP signal was seen (Figure 3, E and F). This suggests that PF20 appears to be preferentially lost from Δ*LmxFused* and Δ*LmxULK4* axonemes. In the reciprocal experiments, KO of *LmxPF20* did not appear to impact either LmxULK4::mNG or LmxFused::mNG expression or localization (Supplemental Figure S4).

Consistent with these findings, cross-sections through free flagella imaged by transmission electron microscopy (TEM) showed normal 9+2 microtubule arrangements and PFR structures in the majority of flagella (Figure 4A, i–iii). No obvious CP defects were noted in any of these TEM profiles, consistent with the observed RSP11::eYFP and PF16::mStr signals in the majority of external flagella and despite the reduction of PF20 signal (Figure 3). Because less than 1% of cells in both Δ*LmxFused* and Δ*LmxULK4* populations showed a noncontinuous or absent PF16::mStr signal (Figure 3B), the number of external flagella assessed by TEM was likely too small to capture those rare cells. We also noted that one out of the 13 Δ*LmxFused* flagella captured by TEM displayed a 10+2 microtubule arrangement (Figure 4Aiv), indicating that a variety of ultrastructural defects may be present within subsets of these long external flagella.

Because fluorescence microscopy data showed that ~25% of KO cells possessed a short flagellum that failed to extend significantly beyond the neck region of the flagellar pocket (Figure 3, iii and iv), the structure of axonemes inside the flagellar pocket was examined next. Here, only 38% of Δ*LmxFused* and 27% of Δ*LmxULK4* axonemes viewed by TEM showed a 9+2 MT arrangement, compared with 100% in the parental controls (Figure 4, B and C). A variety of defects were noted in both CP and outer microtubule doublet number and orientation (Figure 4, B and C), including mispositioned outer doublet MT (Figure 4Biii), <9 doublet MTs (Figure 4B, v and vi), and absence of CP singlet MTs (Figure 4B, iv and vi). The proportion of axoneme sections lacking a CP (Figure 4C) was consistent with the absence of a PF16::mStr signal in about half of the short axonemes viewed by fluorescence microscopy (Figure 3B). To understand better where the defects originated, serial TEM sections spanning the basal body, transition zone, and axoneme regions were examined (Supplemental Figure S5, A–E). Some cells extended only a few singlet or doublet microtubules from a basal body (Supplemental Figure S5,B and C); such cells were likely scored as lacking axonemes entirely in Figure 3 (category v in Figure 3B). Other cells had more subtle defects, showing alteration of MT numbers or positioning (Supplemental Figure S5, D and E). Taking the data together, this suggests that all MT structures of the flagellum are sensitive to the loss of *LmxFused* and *LmxULK4* but none is strictly dependent on these proteins for their formation.

IFT recruitment and processivity correlates with Δ*LmxFused* and Δ*LmxULK4* flagellar morphotype

To determine whether the loss of *LmxFused* and *LmxULK4* affected IFT, two cell lines were generated that expressed fluorescently tagged IFT proteins, mNG::IFT81/LmxM.33.0230 and mNG::IFT140/LmxM.31.0310 (components of the IFT-B and IFT-A subcomplexes, respectively [Nakayama and Katoh, 2018]). *LmxFused* and *LmxULK4* were then knocked out in these reporter lines, which presented with the typical flagellar abnormalities described above. In the minority population that still possessed a long flagellum, IFT particle numbers and velocity were measured, and the results showed that the trains migrated at a relatively normal velocity along Δ*LmxFused* and Δ*LmxULK4* flagella (Supplemental Figure 6, A–N). This analysis demonstrates that in the absence of *LmxFused* and *LmxULK4* at least some cells retain the capacity for normal IFT in fully grown flagella and does not preclude the possibility that loss of *LmxFused* or *LmxULK4* KO could directly impede IFT in newly growing flagella or in the cells that fail to construct an axoneme at all. Indeed, examination of the fluorescent signals showed that a minority population of Δ*LmxULK4* and Δ*LmxFused* cells did not have IFT signal foci in the basal body region. The mNG::IFT81 signal was absent in 6% of Δ*LmxFused* cells and in 7% of Δ*LmxULK4* cells; the mNG::IFT140 focus at the flagellum base was absent in 37% of Δ*LmxFused* cells and in 28% of Δ*LmxULK4* cells (Supplemental Figure S6, O and P). Taken together, these data show that the IFT behavior in Δ*LmxFused* and Δ*LmxULK4* cells correlated with the flagellar morphotype. It remains to be tested whether this apparent reduction in IFT protein recruitment is caused by the loss of LmxFused or LmxULK4, and thus a primary cause of flagellum assembly failure, or whether reduced IFT recruitment is an indirect downstream consequence of structural defects resulting from *LmxFused* and *LmxULK4* KO loss.

Δ*LmxULK4* mutants display reduced α-tubulin acetylation, though Δ*LmxFused* mutants do not

A recent study showed that RNA interference (RNAi)-mediated knockdown of *ULK4* resulted in reduced levels of acetylated α-tubulin in both primary cultured mouse neurons and brain sections (Lang *et al.*, 2016), though that study did not examine cilia or flagella directly. α-Tubulin acetylation has previously been linked to increased microtubule stability and flexibility (see Janke and Montagnac, 2017; Portran *et al.*, 2017). To test the α-tubulin acetylation levels in the *L. mexicana* parental and KO cell lines, cells were stained with antibody C3B9. This revealed a strong signal along the length of the flagellum and a cortical cell body signal, indicating detection of acetylated tubulin in the axonemal microtubules as well as in the cortical cytoskeleton (Figure 5A). Knockout of *LmxULK4* resulted in a reduction in acetylated α-tubulin signal in both the *Leishmania* cell body and flagellum (Figure 5, A and B). That signal was restored upon expression of an episomal add back copy of *LmxULK4* (Figure 5, A and B). However, no such reduction in acetylated α-tubulin was noted in the Δ*LmxFused* cell line (Figure 5, A and B). As a control, we knocked out *LmxαTAT1* (LmxM.25.1150), the orthologue of the dominant mammalian α-tubulin acetyltransferase. These cells showed a near complete loss of acetylated α-tubulin signal (Figure 5, A and B). Interestingly, however, these

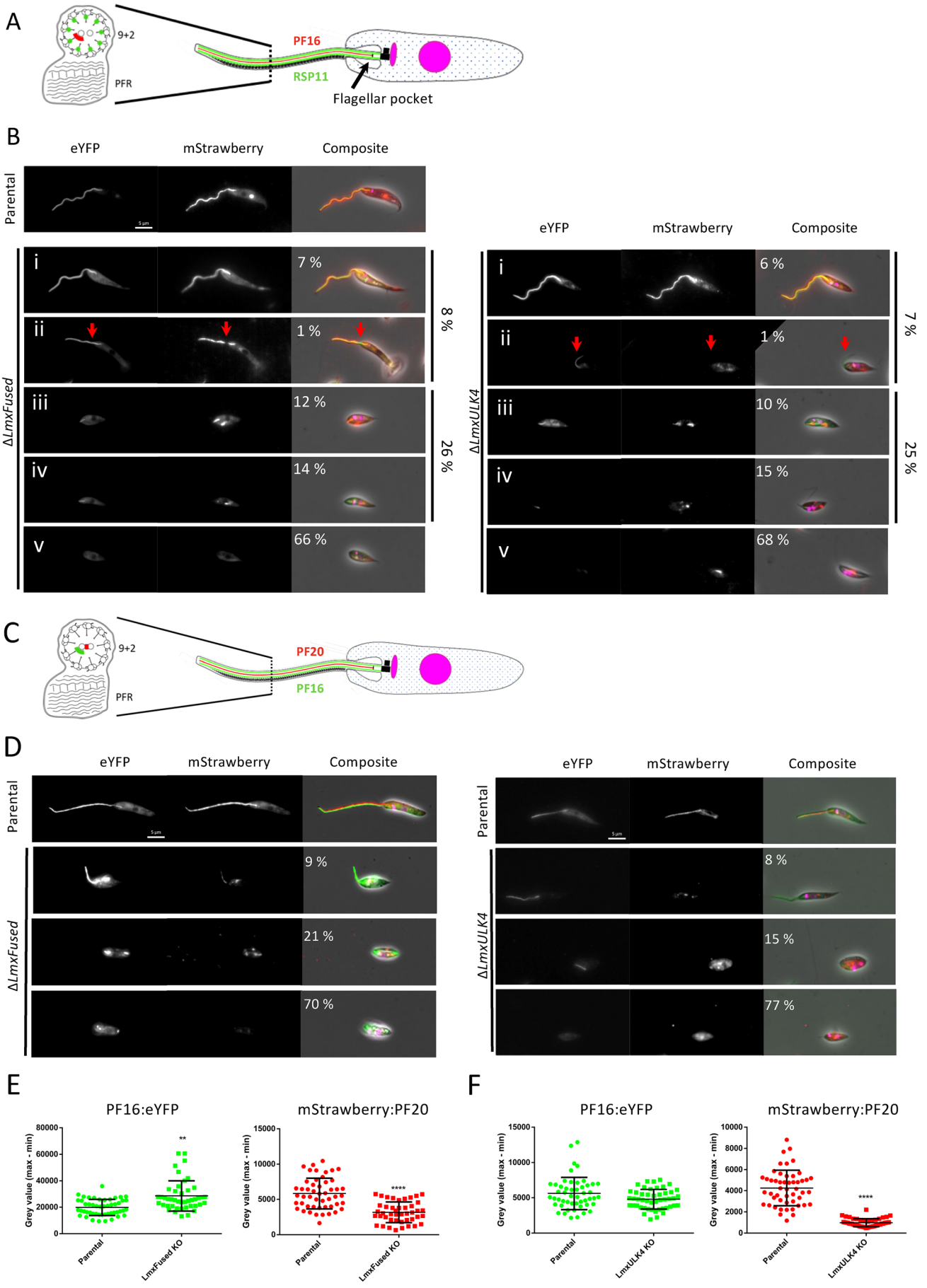
A
9+2
PFR
PF16
RSP11
Flagellar pocket
B
eYFP
mStrawberry
Composite
Parental
ΔLmxFused
i
ii
iii
iv
v
7 %
1 %
12 %
14 %
66 %
8 %
26 %
ΔLmxULK4
6 %
1 %
10 %
15 %
68 %
7 %
25 %
C
9+2
PFR
PF20
PF16
D
9 %
21 %
70 %
8 %
15 %
77 %
E
PF16:eYFP
mStrawberry:PF20
Grey value (max - min)
Parental
LmxFused KO
F
LmxULK4 KO

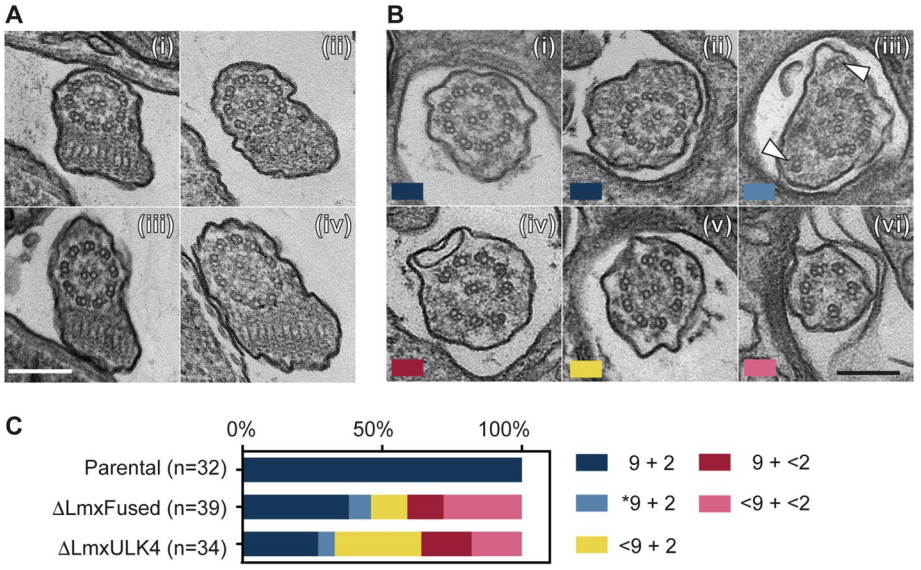

FIGURE 4: Ultrastructural defects in Δ*LmxFused* and Δ*LmxULK4* axonemes. Transmission electron microscopy images showing cross-sections of flagellar axonemes. (A) Sections through the distal part of the flagellum outside of the flagellar pocket: (i) parental, (ii) Δ*LmxULK4*, (iii, iv) Δ*LmxFused*. (B) Sections through the proximal part of the flagellum within the flagellar pocket show examples of normal 9 + 2 microtubule arrangements in (i) parental and (ii) Δ*LmxFused* flagella and examples of ultrastructural defects in Δ*LmxFused* (iii–vi). Color labels indicate categories as quantified in C. (C) Quantification of ultrastructural defects of axonemes within the flagellar pocket (parental control [$n = 32$]; Δ*LmxULK4* [$n = 34$]; Δ*LmxFused* [$n = 39$]; each cell line was analyzed once). The categories were based on the number and arrangement of microtubules (MT). 9+2 (dark blue) represents the normal configuration of nine radially symmetric outer doublet MTs and two singlet MTs; *9+2 indicates a collapse in the radial symmetry (light blue); <9+2 (yellow), 9+<2 (dark pink), and <9+<2 (light pink) indicate deviations from the expected MT numbers.

cells possessed normal long flagella (Figure 5C) and swam normally when observed in culture. Taken together, these data show that the level of α-tubulin acetylation did not correlate with the capacity to build normal motile flagella in these *Leishmania* mutants and that the flagellar defects seen in Δ*LmxFused* and Δ*LmxULK4* cell lines were not caused by a reduction in tubulin acetylation. ULK4 may instead regulate α-tubulin acetylation in a Fused/STK36-independent manner in *Leishmania* and perhaps mammals as well (Lang *et al.*, 2016).

Interaction between *LmxULK4* and *LmxFused*

The similarities of the Δ*LmxFused* and Δ*LmxULK4* flagellar phenotypes individually and in combination (see Figures 2–4) suggest that *LmxFused* and *LmxULK4* may act in a common pathway. To determine whether they are in close spatial proximity and to identify other proximal proteins or complexes, we tagged both alleles of *LmxFused* with the promiscuous *Escherichia coli*–derived biotin ligase BirA* and preformed proximity-dependent biotinylated protein identification (BioID [Roux *et al.*, 2012]). Expression of LmxFused::BirA* had no effect on the growth of the cells in culture (Supplemental Figure S7A), and the protein showed the expected localization (Supplemental Figure S7B). Biotinylated proteins were captured with streptavidin-coupled beads and Western blot analysis confirmed the presence of the bait protein LmxFused::BirA* in the eluted fraction (Supplemental Figure S7C), which was then analyzed by nano-LC/MS/MS. The parental cell line subjected to the same pull down and MS analysis served as a control. As expected, several endogenously biotinylated proteins (putative carboxylase subunits) were identified and highly represented in both samples (Supplemental Data File 1). We used SINQ analysis (Trudgian *et al.*, 2011) to test for enrichment of biotinylated proteins in the LmxFused::BirA* line and identified 125 enriched proteins (Supplemental Data File 1): 47 were detected only in the LmxFused::BirA* sample (Supplemental Data File 1 and Figure 6A), and 78 proteins showed ≥2-fold enrichment within the LmxFused::BirA* sample (Supplemental Data File 1 and Figure 6B). Notably, LmxULK4 was the most highly represented protein identified specifically within the LmxFused::BirA* sample after the bait protein itself (Figure 6A), suggesting that these proteins are in close proximity to each other in the cell. To test whether there was direct physical interaction between LmxFused and LmxULK4, we

FIGURE 3: Quantification of distinct flagellar morphotypes in *LmxULK4* and *LmxFused* KO lines. (A) Cartoon depicting the expected flagellar localization of fluorescently labeled RSP11::eYFP (green) and PF16::mStr (red) within the parental cell line. (B) Micrographs showing an example of each distinct flagellar morphotype observed in the tagged cell line (parental) and upon deletion of *LmxFused* (left panel) or *LmxULK4* (right panel) (500 individual cells counted per cell line; each cell line was analyzed once). Flagellar morphotypes were defined as follows: (i) a long external flagellum with no apparent defect, (ii) a long flagellum with reduced or noncontinuous PF16::mStr signal (highlighted by red arrows), (iii) a flagellum restricted to the flagellar pocket, (iv) a flagellum restricted to flagellar pocket lacking PF16::mStr signal, or (v) no flagellar structure detected, as assessed by the absence of fluorescently labeled proteins at the anterior cell pole where the flagellum normally emerges. (C) Cartoon depicting the expected flagellar localization of PF16::eYFP (green) and mStr::PF20 (red) within the parental cell line. (D) Micrographs showing an example of each distinct flagellar morphotype observed in the tagged cell line (parental) and upon deletion of *LmxFused* (left panel) or *LmxULK4* (right panel) (500 individual cells counted per cell line; each cell line was analyzed once). The composite images in B and D are overlays of the phase-contrast image with the red and green fluorescence channels and the Hoechst 33342 fluorescence indicating nuclear and kinetoplast DNA. (E, F) Comparison of flagellar PF16::eYFP and mStr::PF20 signal intensity in the parental cell line ($n = 50$) with Δ*LmxFused* ($n = 44$) (E) and Δ*LmxULK4* ($n = 48$) (F) cell lines. This analysis included only cells with a long external flagellum with a continuous PF16::eYFP signal (two-tailed Mann–Whitney tests [$^{**}P \leq 0.01$; $^{****}P \leq 0.0001$; mean ± SD]; each cell line was analyzed once).

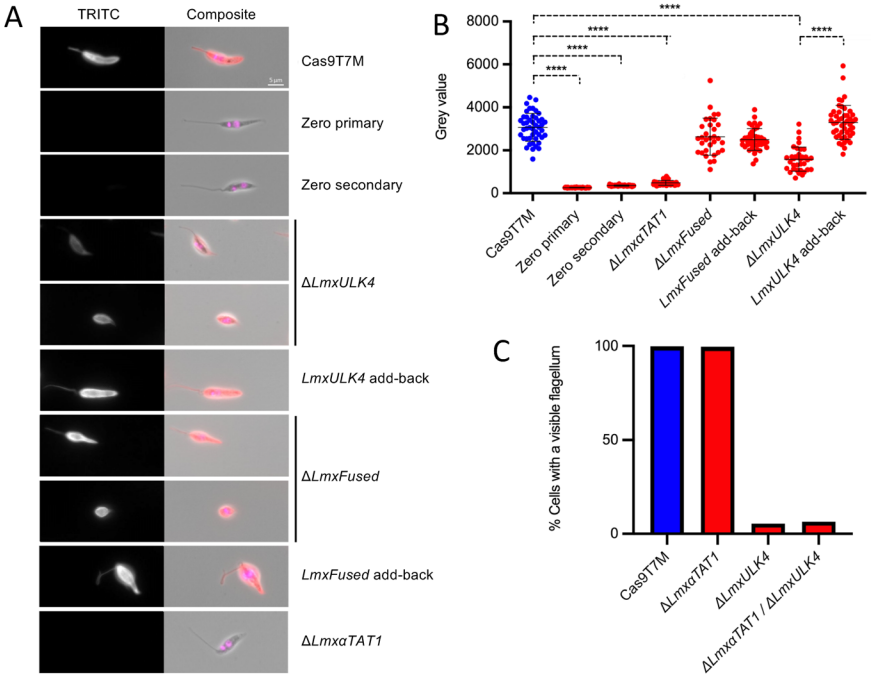

FIGURE 5: Acetylated α-tubulin levels in ΔLmxULK4 and ΔLmxFused cell lines. (A) Acetylated α-tubulin was detected via immunofluorescence using monoclonal antibody C3B9 and TRITC-conjugated secondary antibody. DNA was labeled with Hoechst 33342. (B) Comparison of flagellar TRITC signal intensity between the parental ($n = 46$), zero primary ($n = 39$), zero secondary controls ($n = 45$), the Δ*LmxULK4* ($n = 36$), Δ*LmxFused* ($n = 32$), and Δ*LmxαTAT1* ($n = 38$) deletion mutants, and *LmxULK4* ($n = 48$) and *LmxFused* ($n = 44$) add back cell lines. For Δ*LmxULK4* and Δ*LmxFused*, cells that displayed a long external flagellum were included in the analysis (Kruskal–Wallace test with Dunn's correction for multiple comparisons [$^{****}P \leq 0.0001$; mean ± SD]; each cell line was analyzed once). (C) Percentage of cells displaying a visible long external flagellum that extends beyond the flagellar pocket in the parental cell line (99.8%) populations of Δ*LmxαTAT1* (99.6%) Δ*LmxULK4* (5.4%), and Δ*LmxULK4*/Δ*LmxαTAT1* (6.4%) (500 individual cells counted per cell line; each cell line was analyzed once).

performed immunoprecipitation (IP) in a cell line expressing LmxFused::eYFP and LmxULK4::MYC. Expression of fusion proteins was confirmed by fluorescence imaging (LmxFused::eYFP; Supplemental Figure S8A) and Western blots of whole cell lysates (both proteins; Supplemental Figure S8, B and C). Cell lysates were incubated with anti-GFP–conjugated beads, and protein pull down of LmxFused::eYFP was confirmed by Western blot (Supplemental Figure S8B). A control cell line expressing GFP served as a control for the pull-down and MS analyses (Supplemental Figure 8D). The eluates were analyzed by mass spectrometry (Supplemental Data File 2). The two highest scoring hits were a carbamoyl-phosphate synthase (LmxM.16.0590) and LmxULK4. Notably, 29 of 30 ULK4 peptides mapped specifically to the N-terminus of LmxULK4 (Supplemental Figure S8E), within the first 340 of 1315 amino acids. Western blots probing for the C-terminal tag on LmxULK4::MYC suggested that the protein was cleaved or degraded following cell lysis (Supplemental Figure S8C). The detection of peptides derived from the LmxULK4 N-terminus in IP eluates is consistent with a direct physical interaction between LmxFused and the N-terminal region of LmxULK4. This is consistent with proximity-labeling data showing interactions only with the N-terminal pseudokinase domain of mammalian ULK4 with Fused/STK36 but not with the ULK4 C-terminal domains (Preuss *et al.*, 2020).

Given the data presented above supporting an interaction between LmxFused and LmxULK4, we investigated the impact of gene KOs for one of these proteins on the subcellular localization of the other protein. *LmxULK4* KO did not appear to affect LmxFused::mNG localization (Figure 6D). In the equivalent reciprocal experiment, the signal from LmxULK4::mNG (both alleles tagged) disappeared upon deletion of *LmxFused*, suggesting that the stable expression of LmxULK4 was dependent on the presence of LmxFused (Figure 6E). These data further corroborate the KO phenocopy and together with the LmxFused BioID and Co-IP results, which both identified LmxULK4 as a high-scoring interaction partner, support the hypothesis that LmxULK4 and LmxFused physically and functionally interact to contribute to the assembly of a normal motile eukaryotic flagellum.

Interactions with other flagellar proteins

The targets of the LmxFused kinase remain unknown. BioID and Co-IP both identified additional proteins, albeit with little overlap between the two methods (Supplemental Data Files 1 and 2). Of the 24 proteins identified in the Co-IP with LmxFused::eYFP (≥3 spectral counts), 15 were also coimmunoprecipitated with the soluble GFP pull-down control sample, suggesting that these proteins directly interact with eYFP tag as opposed to LmxFused itself (Supplemental Data File 2). Besides LmxULK4, there were only six proteins detected with >2 peptides in the LmxFused Co-IP sample (and < 2 peptides in the GFP pull-down and parental control samples): LmxM.16.0590 (putative carbamoyl-phosphate synthase), LmxM.11.0940 and LmxM.26.1450 (both hypothetical proteins, present in the flagellar proteome [Beneke *et al.*, 2019]), LmxM.36.4330 (the *L. mexicana* orthologue of *T. brucei* flagellar attachment zone [FAZ] protein FAZ22 [Zhou *et al.*, 2018]), and LmxM.08_29.2510 (glycosomal ATP-dependent 6-phosphofructokinase) and LmxM.30.1910 (hypothetical protein) (Figure 6C). Further experiments are required to establish which, if any, of these are genuine interaction partners of LmxFused/LmxULK4.

In addition to identifying components of a protein complex, BioID could provide information about the subcellular domains where LmxFused resides, identifying proteins that do not directly interact with LmxFused but that are in close proximity to it. Besides LmxULK4, the 124 enriched proteins included 23 that have been previously identified within the *L. mexicana* flagellar proteome (Beneke *et al.*, 2019) and seven that associate with the FAZ, consistent with the observed subcellular localization pattern of LmxFused. We hypothesized that potential substrates of LmxFused or direct interaction partners may be found among the most highly enriched proteins in the LmxFused::BirA* sample. We used gene KO to determine whether deletion of these genes had a similar effect as loss of Fused and whether a dual KO modulated the Δ*LmxFused* phenotype, as assessed by quantifying the proportion of cells with a long flagellum (Figure 6F). We included in this experiment the proteins that were identified only in the LmxFused::BirA* sample with ≥4 spectral

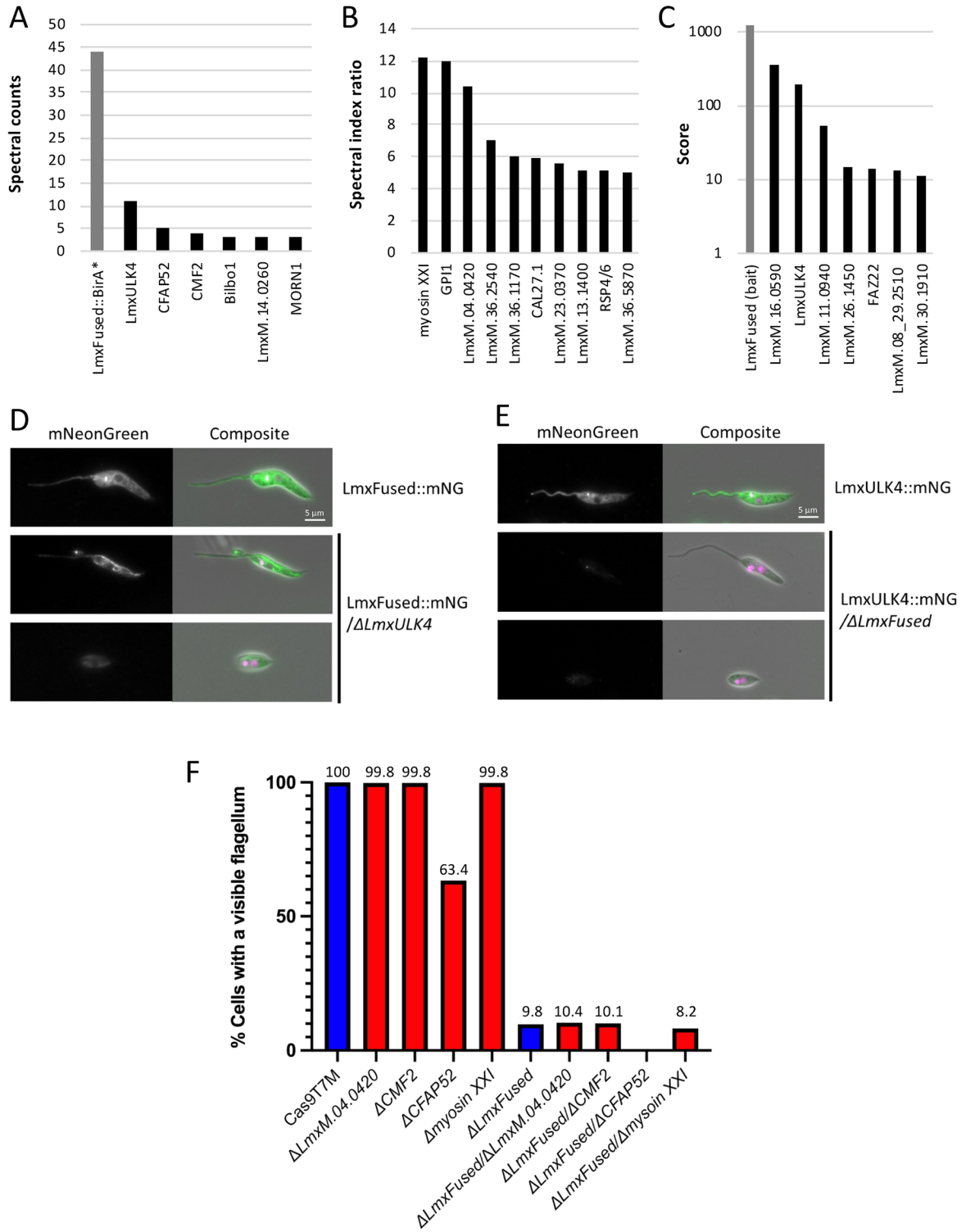

FIGURE 6: BioID and IP data support an interaction between LmxFused and LmxULK4. (A) Proteins that were identified by BioID only in the LmxFused::BirA* samples. (B) Proteins identified by BioID that were ≥ 5-fold enriched within the LmxFused::BirA* samples relative to the parental control (Cas9T7M). (C) Proteins that coimmunoprecipitated with LmxFused::eYFP and for which ≤1 peptides were identified in the parental or GFP control sample. (D) Visualization of LmxFused::mNG in live promastigotes before and after the deletion of *LmxULK4*. (E) Visualization of LmxULK4::mNG in live promastigotes before and after deletion of LmxFused. The composite images show overlays of phase-contrast images with the green fluorescence channels and fluorescence of Hoechst 33342 to indicate nuclear and kinetoplast DNA. (F) The percentage of cells displaying a visible long external flagellum that extends beyond the flagellar pocket was quantified in promastigote populations following KO of myosin XXI, LmxM.04.0420, CFAP52, or LmxM.27.0870 (CMF2) individually or in combination with KO of LmxFused (500 individual cells counted per cell line; each cell line was analyzed once).

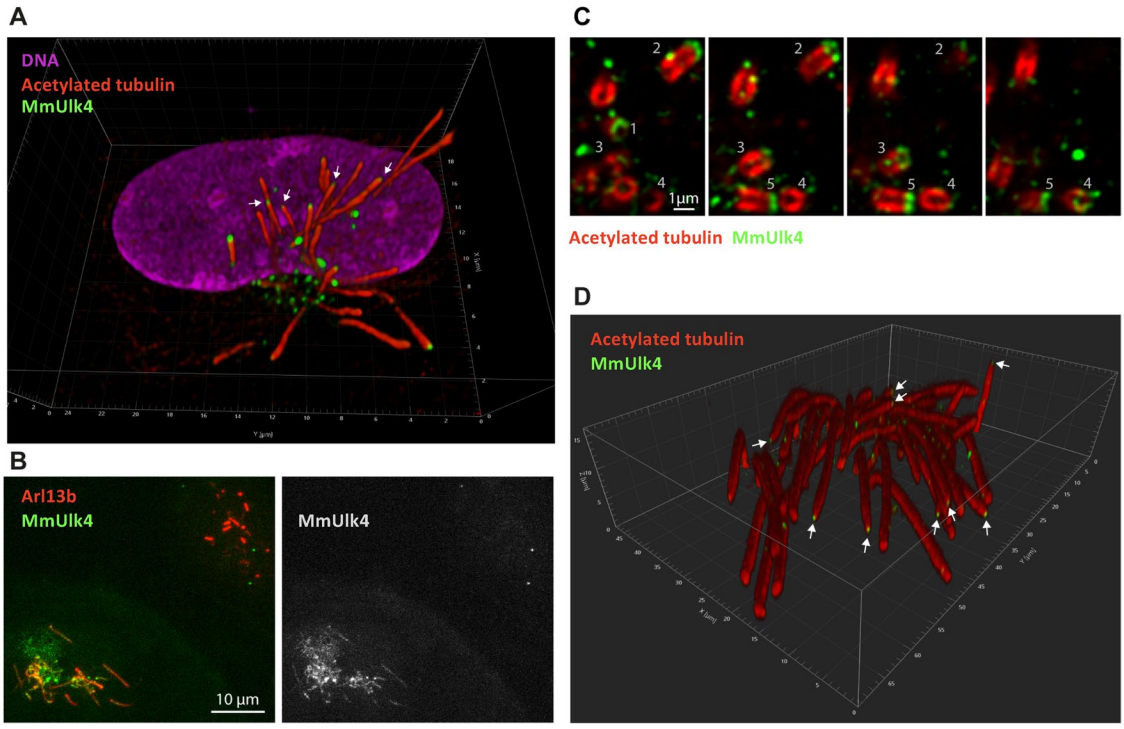

FIGURE 7: Localization of ULK4 in mouse ependymal cilia. (A) Immunofluorescence staining of a multiciliated mouse ependymal cell. 3D reconstructed confocal z-stack using Imaris viewer (blend mode). Z-step size was 130 nm. Acetylated tubulin (labeled with C3B9) in red, Flag-HA-mNeonGreen–tagged MmULK4 (mNG fluorescence) in green, DNA (DAPI) in magenta. Note the strong mNG signal at tips of short axonemes and the weaker signal associated with tips of certain longer axonemes (arrows). Note that under used conditions the anti-acetylated antibody does not label centrioles in immunofluorescence. (B) Maximum-intensity projection of confocal z-stack encompassing the apical region of two multiciliated cells, one expressing Flag-HA-mNeonGreen–tagged MmULK4 (bottom left) and the other not (top right). To improve the signal-to-noise ratio, we used 4× line averaging. Raw data are presented. Left: ciliary marker Arl13b (labeled with anti-Arl13b antibody) in red, Flag-HA-mNeonGreen–tagged MmULK4 (mNG fluorescence) in green. Right: mNG signal only. (C) Selected confocal planes of an apical region of an expanded multiciliated mouse ependymal cell, which encompasses centrioles. Individual planes are separated by 700 nm in the axial direction. Individual centrioles (labeled with C3B9; in red) are denoted with numbers. Note the Flag-HA-mNeonGreen–tagged MmULK4 signal (anti-HA staining; in green) capping one end of each centriole. (D) 3D reconstruction of a confocal z-stack encompassing distal parts of cilia of an expanded multiciliated mouse ependymal cell. Z-step size was 100 nm, and Imaris viewer (blend mode) was used for the reconstruction. Acetylated tubulin (labeled with C3B9) in red, Flag-HA-mNeonGreen–tagged MmULK4 (anti-HA signal) in green. Arrows indicate the tips of axonemes with detectable MmULK4.

counts (LmxM.28.1110, Cilia And Flagella Associated Protein 52 [CFAP52], and LmxM.27.0870, Component of Motile Flagellum 2; [CMF2]) and those that were highly enriched in the LmxFused::BirA* sample compared with the control (spectral index ratio ≥10; LmxM.31.3870 [putative myosin XXI], LmxM.08_29.2030 [putative N-acetylglucosamyl transferase component GPI1], and LmxM.04.0420 [tetratricopeptide repeat protein]). Loss of myosin XXI, LmxM.04.0420, and LmxM.27.0870 (CMF2) either individually or in combination with Δ*LmxFused* did not alter the phenotype of the respective parental cell line (Figure 6F). For GPI1 this could not be assessed, as we were unable to generate a null mutant. By contrast, KO of *LmxCFAP52* alone resulted in a 37% reduction in cells exhibiting long external flagella. Interestingly, the Δ*LmxFused*/Δ*LmxCFAP52* dual KO resulted in cells that lacked long external flagella entirely (Figure 6F), exacerbating the phenotype of the individual gene deletions. *Chlamydomonas* FAP52 was recently shown to function in the stabilization of axonemal microtubules (Owa *et al.*, 2019). One possible interpretation of the KO phenotypes observed here in *L. mexicana* is that flagellar stability is compromised to different degrees by the loss of CFAP52 and the loss of LmxFused, and when both are lost together, cells can no longer build any flagella.

Mammalian ULK4 localizes to motile cilia of mouse ependymal cells

Previous studies have provided several strong lines of evidence linking mammalian Fused/STK36 and ULK4 to motile cilia function (Wilson *et al.*, 2009; Liu *et al.*, 2016), and biochemical evidence indicated the proximity of mammalian Fused/STK36 and ULK4 (Preuss *et al.*, 2020). Mammalian Fused/STK36 was shown to localize along the entire length of the motile cilia (Nozawa *et al.*, 2013), but the localization of mammalian ULK4 to motile cilia has not been assessed. We therefore transiently expressed mouse ULK4 (MmULK4) tagged with Flag-HA-mNeonGreen in the primary cell culture of mouse ependymal cells competent of forming motile cilia; aberrant axonemal structure was previously observed in this cell type of *ULK4* hypomorph mice (Liu *et al.*, 2016). Staining fixed cells with an antibody against acetylated tubulin as an axonemal marker revealed that the tagged MmULK4 localized to multiple foci in the apical region of the cell, in which the cilia originated, and at distal tips of short axonemes (Figure 7A). An accumulation, albeit with lower signal intensity, was noticeable also at the tips of a subset of longer axonemes. Finally, a weak but discernible signal was observed along each axoneme and a diffused signal in the cytosol (Figure 7B).

We next wanted to assess whether the dot-like signals in the apical region could be associated with centrioles. As the combination of the anti–acetylated tubulin antibody and formaldehyde fixation was well suited for the visualization of axonemes in immunofluorescence, but not for centrioles, we used expansion microscopy, which was previously shown to facilitate access of antibodies to their respective epitopes (Tillberg *et al.*, 2016). Following the ultrastructure expansion microscopy protocol from Gambarotto *et al.* (2019) we achieved about 4.7-fold expansion. Indeed, we observed that centrioles in the apical region, which did not extend axonemes, had the Flag-HA-mNeonGreen-MmULK4 associated with them, as determined by anti-HA staining (Figure 7C). The signal was always juxtaposed distal to one end of the centriole as defined by the anti–acetylated tubulin signal (Figure 7C). Moreover, expansion microscopy confirmed that Flag-HA-mNeonGreen-MmULK4 was present at the very tips of a subset of long axonemes (Figure 7D).

Taken together, our data support a function for ULK4 and Fused/STK36 in motile cilia from evolutionarily distant cells and suggest a model in which ULK4 and Fused/STK36 interact with each other to enable stable assembly of motile flagella and cilia across eukaryotic cells.

DISCUSSION

Here we characterized the phenotypic consequences of *Fused/STK36* and *ULK4* KO on motile flagellum assembly in the protozoan *L. mexicana*. We found that Δ*LmxULK4* and Δ*LmxFused* cells lines display equivalent flagellar defects and as such effectively phenocopy each another (Figures 2 and 3) and suggest that they function within the same pathway. Intriguingly, the severity of flagellar structure defects varied between cells within KO populations (Figures 2–4), and yet the proportion of distinct flagellar morphotypes remained consistent across multiple independent deletions of both genes and in different parental cell lines (Figures 2 and 3 and Supplemental Figure S6). These data are consistent with the loss-of-function phenotypes described by Baker *et al.* (2021) in a KO screen of *Leishmania* kinases. Furthermore, they suggest that the proteins are involved in regulating ciliogenesis or ciliary stability but are not essential for the initiation of flagellar growth. The fact that in a minority of cells flagella were still present was informative, as these allowed us to detect a pattern of defects that are consistent with a progressive collapse of the axoneme either during or after assembly. In contrast, RNAi-mediated knockdown of Fused and ULK4 in the related protist *T. brucei* (Jones *et al.*, 2014; Varga *et al.*, 2017) did not affect assembly of stable flagella. A small proportion of cells in which FCP6/TbFused was knocked down showed evidence of aberrant cytokinesis, which may be linked to perturbation of motility (Varga *et al.*, 2017). The differences in the severity of phenotype between *L. mexicana* and *T. brucei* may be a result of the distinct reverse genetics methods employed (i.e., gene KO vs. knockdown). Alternatively, they could suggest that *T. brucei* possesses an unknown compensatory failsafe mechanism that results in increased flagellar assembly robustness when faced with Fused or ULK4 functional perturbation. A third possibility is that there is some divergence between Fused and ULK4 functions in *T. brucei* and *L. mexicana* that could be linked to the differences in cellular architecture. *T. brucei* flagella have extensive structural connections to the cell body, and the newly assembling flagellum is linked to the existing flagellum through the FC structure where Fused or ULK4 were localized. The *L. mexicana* flagellum is connected only in its proximal part to the cell body, via a FAZ structure (Wheeler *et al.*, 2016) and lacks a recognizable FC structure.

In addition to the phenocopy of Δ*LmxFused* and Δ*LmxULK4* described above, we show that LmxFused and LmxULK4 are in close proximity to one another (LmxFused::BirA*-mediated BioID; Supplemental Data File 1; Figure 6A) and they coimmunoprecipitate (via LmxFused::eYFP pull down; Supplemental Data File 2; Figure 6C), and the stable expression of LmxULK4::mNG is dependent on the presence of *LmxFused* (Figure 6E). Together these data suggest that LmxULK4 and LmxFused function as part of the same pathway to mediate stable flagellum assembly or maintenance in *Leishmania*. Although Fused/STK36 and ULK4 have not yet been shown to directly interact in mammals, both *Fused/STK36* and *ULK4* mutants are associated with a range of motile cilia assembly defects in distinct mouse tissues (Wilson *et al.*, 2009; Vogel *et al.*, 2012; Nozawa *et al.*, 2013; Liu *et al.*, 2016). Mammalian Fused/STK36 was previously shown to localize to the motile cilium (Nozawa *et al.*, 2013), and we now demonstrated localization of MmULK4 to motile cilia of ependymal cells (Figure 7). Its pattern is indeed reminiscent of the pattern of LmxULK4; MmULK4 localizes along the cilium with enrichment at the distal tip of the axoneme. Moreover, the accumulation at tips of nascent cilia resembles the situation in *T. brucei*, where the orthologue FCP5/TbULK4 localizes to the flagella connector present at the tip of growing flagella (Varga *et al.*, 2017). These finding point to a remarkable conservation of localization of the protein in evolution and make *Leishmania* a tractable model to dissect the mechanisms by which Fused/STK36 and ULK4 contribute to stable flagellum assembly. Interestingly, mammalian ULK4 (tagged with BirA*) has recently been shown to be in close proximity to Fused/STK36 in modified HEK 293T cells (Preuss *et al.*, 2020), supporting the conservation of an evolutionarily ancient Fused/STK36 and ULK4 interaction that likely contributed to the assembly of motile flagella/cilia in the last common ancestor of *Leishmania* and mammals.

To date, relatively little is known about the mechanism through which either protein contributes to stable flagellar assembly. However, the mouse Fused/STK36 orthologue has been shown to coimmunoprecipitate with the flagella/cilia-associated proteins PF20, KIF27, and PCDP1 when expressed in a HEK 293T cell line (Wilson *et al.*, 2009; Nozawa *et al.*, 2013). Of these three established Fused interactors, only the CP-associated protein PF20 has an obvious orthologue in *L. mexicana*. Although LmxPF20 was not shown here to be in close proximity to LmxFused::BirA* or coimmunoprecipitate with LmxFused::eYFP, we did find that Δ*LmxULK4* and Δ*LmxFused* cells exhibited reduced levels of LmxPF20 in their long external flagella, where present (Figure 3). When considered alongside the other CP defects noted in Δ*LmxULK4* and Δ*LmxFused* (Figures 3B and 4), these data support the idea that both ULK4 and Fused/STK36 contribute to normal CP microtubule assembly or maintenance as proposed for mammalian cilia (Wilson *et al.*, 2009; Nozawa *et al.*, 2013; Liu *et al.*, 2016). In some of those mammalian cilia the loss of ULK4 and Fused affected the integrity of the axoneme more widely, however, and in *Leishmania*, the disruption of the outer doublet microtubule arrangements and reduction of flagellar length were the dominant features of the mutant cells.

In addition to LmxULK4, several flagellar proteins were identified within our LmxFused::BirA* BioID data set (see Supplemental Data File 1) as candidate LmxFused interactors. It is interesting to note that CFAP52 and CMF2 were the third and fourth most highly represented proteins identified specifically within the LmxFused::BirA* sample, after only LmxULK4 and the bait proteins itself (Figure 6). Homologues of both CFAP52 (FAP52) and CMF2 (RIB72) in *Chlamydomonas* are microtubule inner proteins (MIPs) that are bound to the inner lumen wall of B and A tubules of the axonemal outer microtubule doublets, respectively (Ma *et al.*, 2019). Both proteins

contribute to enhanced microtubule stability against mechanical stress/damage (Stoddard *et al.*, 2018; Owa *et al.*, 2019), and human patients lacking CFAP52 (also known as WDR16) display laterality abnormalities associated with motile cilia dysfunction (e.g., situs inversus totalis [Ta-Shma *et al.*, 2015]). The identification of these proteins in our BioID data set suggests that LmxFused::BirA* may directly or indirectly interact with one or multiple MIPs to promote microtubule stabilization. In support of this hypothesis, we have established a genetic interaction between *LmxCFAP52* and *LmxFused*, where Δ*LmxFused*/Δ*LmxCFAP52* cells display an exacerbated flagellar assembly defect relative to Δ*LmxFused* alone (they fail to build any long external flagella; see Figure 6F). FAP52 has been described as an interaction hub for a larger MIP network that includes inner junction proteins and also crosses the connection between protofilaments A12 and A13 to interact with the N-terminus of RIB72 in the A tubule (Ma *et al.*, 2019; Khalifa *et al.*, 2020). Individual components of this MIP network can act synergistically to promote microtubule stability (e.g., FAP52, FAP45, and FAP20 [Owa *et al.*, 2019]), perhaps warranting the examination of further potential genetic interactions between LmxFused and other MIPs. Though not yet proven, LmxFused could interact with MIPs either before their incorporation into the microtubule, via diffusion along the lumen accessed at the microtubule extremities (though the rate of intraluminal diffusion may be limiting; [Janke and Montagnac, 2017]) or through gaining luminal access at random breakage points to promote microtubule repair. Indeed, it is possible that the diversity of flagellar morphotypes described here is in part a result of the stochastic nature of microtubule destabilization events that may occur at a higher frequency and/or remain unrepaired in the absence of LmxFused- and LmxULK4-associated signaling pathways. It is worth noting that CFAP52 has also been localized to the mouse sperm manchette (Tapia Contreras and Hoyer-Fender, 2020), another microtubular structure that was adversely affected upon the loss of Fused (Nozawa *et al.*, 2014).

It should be noted that, apart from LmxULK4, none of the flagellar proteins identified via BioID also coimmunoprecipitated with LmxFused::eYFP. This discrepancy is likely due to the fact that our IP protocol was biased towards the identification of soluble proteins, as we primarily attempted to confirm the interaction between LmxFused and LmxULK4, both of which appear to be detergent extractable (see Supplemental Figure S1). Future efforts to confirm any candidate LmxFused protein kinase substrates identified here could be aided by the generation of a suitable engineered ATP analogue–specific LmxFused kinase (Romano *et al.*, 2017).

Though not directly tested here, ULK4 is predicted to be a pseudokinase (Figure 1B), similar to the metazoan ULK4 proteins. Interestingly, ULK4 in plants and other protists still possesses the canonical catalytically relevant residues and it appears that catalytic activity may have been lost multiple times in evolution (Preuss *et al.*, 2020). LmxFused is predicted to be an active kinase. In *Drosophila* hedgehog signaling, Fused displays both catalytic and noncatalytic functions (see Maloverjan and Piirsoo, 2012. for a review). By contrast, attempts to demonstrate mammalian Fused kinase activity in vitro were unsuccessful [Murone *et al.*, 2000; Wilson *et al.*, 2009]), leading to speculation that the mammalian Fused orthologue may not function as an active kinase (Maloverjan and Piirsoo, 2012). However, given the conservation of canonical catalytically relevant amino acid residues within the active site of these proteins (Figure 1B) and that our results suggest that Fused and ULK4 may function together as a part of the same pathway, it may be interesting to test for mammalian Fused kinase activity in the presence of ULK4.

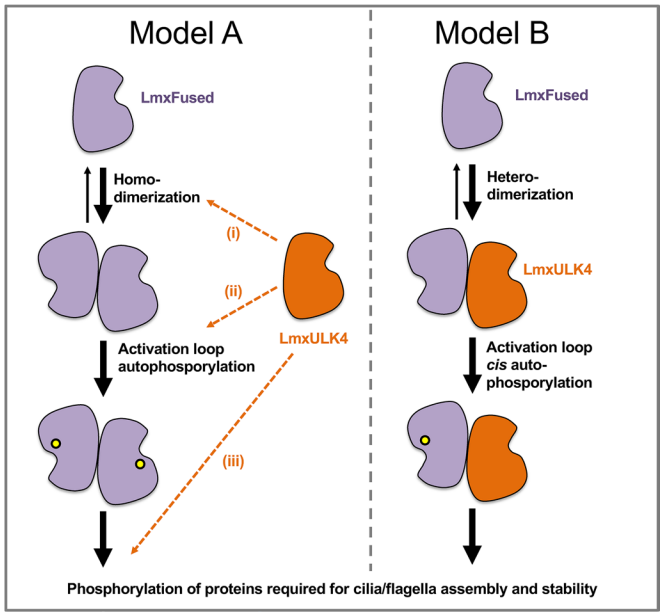

FIGURE 8: Models for possible interactions between ULK4 and Fused/STK36. In model A, LmxFused forms a homodimer and LmxULK4 interacts transiently with LmxFused to promote one or several steps of kinase activation: (i, ii) homodimerization, (iii) activation loop phosphorylation and/or (iii) the interaction of LmxFused with downstream targets. Yellow circles represent activation loop phosphorylation. In model B, LmxFused forms a heterodimer with LmxULK4. Heterodimerization promotes *cis* autophosphorylation of the LmxFused activation loop to contribute to flagellum assembly or microtubule stabilization.

How might ULK4 affect the activity of Fused? Deletions of LmxULK4 KO or LmxFused KO result in the same phenotype with respect to flagellar morphotype (Figures 2–4). In *Leishmania* the dual KO cell line (Δ*LmxULK4*/Δ*LmxFused*) appears phenotypically indistinguishable from either Δ*LmxULK4* or Δ*LmxFused* (Figures 2–4). This argues against an inhibitory function of ULK4. Instead ULK4 may stimulate Fused kinase activity in some way, either through the allosteric activation of Fused kinase activity or functioning as a scaffold to facilitate Fused-substrate interactions that may not otherwise occur at a sufficient rate via diffusion alone (see models in Figure 8). In *Drosophila* (which lacks an ULK4 orthologue) Fused homodimerization precedes *trans* autophosphorylation of the activation loop to promote kinase activity and normal hedgehog signaling (Shi *et al.*, 2011; Zhang *et al.*, 2011). It therefore seems likely that the *Leishmania* orthologue may similarly require both dimerization and activation loop phosphorylation (common protein kinase activation steps) to facilitate LmxFused kinase activity (Figure 8, model A). Indeed, the Fused orthologue in mice appears to oligomerize (Fused proteins tagged with alternate epitopes exhibit Co-IP [Nozawa *et al.*, 2013]), supporting the potential for Fused dimerization (if not multimerization) in mammals as well. Conversely, given the precedent for established pseudokinase-kinase interactions and heterodimers, where the pseudokinase interacting partner regulates the activity of the bona fide catalytic kinase (see Shaw *et al.*, 2014, for a review), it is also possible that LmxFused forms a heterodimer with LmxULK4 (Figure 8, model B). Shaw *et al.* (2014) hypothesize that pseudokinase-kinase heterodimerization may represent a common phenomenon that facilitates *cis* autophosphorylation and precedes kinase activation.

While this study focused on the role of Fused/STK36 and ULK4 with respect to motile flagellum construction and maintenance, this interaction likely has functional relevance beyond motile cilia and flagella structure and function. In support of this idea, and as highlighted above, ULK4 was shown to be in close proximity to both Fused and several other microtubule-associated proteins in HEK 293T cells (Preuss *et al.*, 2020), a cell line that lacks motile cilia. Both proteins also localize to the same layer of the *T. brucei* flagella connector (Varga *et al.*, 2017), though their function within this insoluble mobile transmembrane structure is not yet known. Additionally, although not yet proven experimentally, it has recently been hypothesized that the orthologous proteins of Fused (TIO) and ULK4 (RUK) may cooperate to regulate microtubule depolymerization in the lagging edge of the cytokinesis/cell plate–associated plant phragmoplast (Smertenko *et al.*, 2018). The nonciliated species *Dictyostelium* has a Fused orthologue called *tsunami*, which localizes to microtubules, and *tsunami* mutants have a chemotaxis and polarization defect (Tang *et al.*, 2008). This suggests that interaction with microtubules is an ancestral function of Fused kinases and the interaction between Fused/STK36 and ULK4 appears to represent an evolutionarily ancient partnership that likely contributes to the regulation of microtubule stability or microtubule-associated signaling pathways in diverse cellular contexts in many eukaryotic organisms.

MATERIALS AND METHODS

Cell culture and genetic modifications

L. mexicana promastigotes (WHO strain MNYC/BZ/62/M379) were cultured at 28°C in M199 medium (Life Technologies) supplemented with 2.2 g/l $NaHCO_3$, 0.005% hemin, 40 mM HEPES, and 10% fetal calf serum, pH 7.4 (complete M199). Gene tagging and KO cell lines were generated using CRISPR/Cas9 in the *L. mex* Cas9 T7 cell line (stabilate Cas9 T7 M), as described by Beneke *et al.* (2017) using primer sequences retrieved from www.LeishGEdit.net (see Beneke and Gluenz, 2019), unless specified otherwise. Gene KO was confirmed via diagnostic PCR (see primers included in Supplemental Data File 3) used to assess the presence or absence of the targeted open reading frame (Beneke and Gluenz, 2019). Cells were cultured in the presence of the appropriate selection antibiotics (Beneke *et al.*, 2017); testing for mycoplasma was not routinely done.

Mouse ependymal cell culture was established as described previously (Delgehyr *et al.*, 2015). Briefly, the brain of a P1 mouse (C57Bl/6J) was dissected. Isolated lateral ventricles were mechanically and enzymatically homogenized, and the culture was expanded. Cells were seeded into a poly-L-lysine (Sigma; P1524)-coated eight-well microscopy chamber (Ibidi; 80807) for immunofluorescence assay or onto a poly-L-lysine–coated Ø12 mm microscopy coverslip (Marienfeld; 117520) placed in a 24-well plate for expansion microscopy. A plasmid coding for expression of Flag-HA-mNeonGreen–tagged MmULK4 (cDNA: Origene; MR217918; mNeonGreen; mNG) provided by Allele Biotechnology and Pharmaceuticals (Shaner *et al.*, 2013) under constitutively active CMV promoter was transfected to the seeded cells using Lipofectamine 3000 (Invitrogen; L3000001) following manufacturer instructions. On the following day, the cells were washed twice with DMEM (Sigma-Aldrich; D6429) supplemented with 100 U/ml penicillin (BB Pharma) and 100 µg/ml streptomycin (Sigma-Aldrich; S9137). The cells were incubated in the serum-free medium for 8 d to induce differentiation and ciliogenesis.

Whole genome sequencing

For the original Δ*LmxFused* and Δ*LmxULK4* cell lines, complete gene KO was also confirmed via whole genome sequencing, as described in Beneke *et al.* (2019). Briefly, DNA from mutants was prepared using the Illumina TruSeq Nano DNA library kit, and resulting libraries were quantified using the NEBNext library Quant kit. Library size was determined using the Agilent High Sensitivity DNA kit on a 2100 Bioanalyzer instrument. The quantified library was multiplexed with project-unrelated libraries, spiked with 1% PhiX DNA, and sequenced on a NextSeq 550 (1.8 pM loading concentration). Sequencing was performed in paired-end sequencing mode (2 × 75 cycles, 6 and 8 cycles index read) using a NextSeq 500/550 High Output Kit v2.5 (150 cycles) following the manufacturer's instructions. Genome samples were demultiplexed using bcl2fastq (Illumina), assembled using Burrow–Wheeler Aligner (Li and Durbin, 2009), sorted and indexed using Samtools (Li *et al.*, 2009), and viewed on an integrative genomics viewer (IGV) viewer (Robinson *et al.*, 2011).

Episomal add back

The open reading frame of *LmxFused* was amplified from genomic DNA using primers

F: 5′-TTAGCAACTAGTATGCTTGTGACCATGGAGGACTACC-3′ and

R: 5′-TTAGCAGAATTCTCAGAGGTCCTCCTCGCTAATGAGCTTTTGCTCCAGGTCTTCTTCGCTGATCAGCTTCTGTTCACCAAGTCGATCGACGAGGTTGC-3′

The resultant PCR products were cloned into pTadd (Beneke *et al.*, 2017), using *Spe*I and *Eco*RI restriction sites. The *LmxULK4* add back plasmid was similarly generated using primers

F: 5′-TTAGCAACTAGTATGAACAACTATGTGCTTAATGACGAGATC-3′ and

R: 5′-TTTTCAATTGTCAGAGGTCCTCCTCGCTAATGAGCTTTTGCTCCAGGTCTTCTTCGCTGATCAGCTTCTGTTCGGAGAGTTTCTTCAGAATCTTGTTCGC-3′

and *Spe*I and *Mfe*I restriction sites. Successful cloning was confirmed via Sanger sequencing. Circular plasmid (1 µg) was transfected as described previously (Beneke *et al.*, 2017) to allow episomal expression of LmxFused::2xMYC and LmxULK4::2xMYC. Drug-resistant cells were selected using 25 µg/ml phleomycin.

Live cell microscopy of *Leishmania*

Cells were harvested from log-phase culture by centrifugation (800 × *g*, 5 min), washed once in 1 ml of phosphate-buffered saline (PBS) (containing, if required, 10 µg/ml Hoechst 33342), resuspended in 10 µl of PBS, and imaged live while adhered to a poly-lysine–coated glass slide. Cells were imaged on either a Zeiss Axioimager.Z2 microscope with a 63× numerical aperture (NA) 1.40 oil immersion objective and a Hamamatsu ORCA-Flash4.0 camera or a 63× NA 1.4 objective lens on a DM5500 B microscope (Leica Microsystems) with a Neo sCMOS camera (Andor Technology) at ambient temperature (~25–28°C). Micrographs were processed using Fiji (Schindelin *et al.*, 2012).

Quantification of IFT train migration and parasite motility analysis

IFT fluorescent video micrographs were captured using methods based on those employed by Wheeler *et al.* (2015), with 600 frames captured per video at 50 ms fluorescence exposure per frame (~95 ms delay between frames). IFT particle velocity, intensity, and number were quantified using the publicly available software

KymographClear (ImageJ macro toolset) and *KymographDirect* (see Mangeol *et al.*, 2016), including correction for both background signal and signal bleaching. Short particle tracks were removed from the analyses where necessary to avoid pseudoreplication (multiple measurements of an individual particle). This analysis was restricted to cells that possessed a flagellum that extended significantly beyond the flagellar pocket. Promastigote motility assays using dark-field video microscopy were performed using methods described by Wheeler (2017), including all three modifications outlined by Beneke *et al.* (2019).

Preparation of cells for immunofluorescence

L. mexicana cells were harvested from log-phase culture by centrifugation (800 × *g*, 5 min), washed twice in 1 ml of PBS, and resuspended in PBS at ~3×10^7 cells/ml. Cells were allowed to settle onto a glass slide for 30 min in a humid chamber and fixed in cold methanol (20 min at –20°C). Samples were rehydrated and washed twice in PBS before antibody labeling. Immunofluorescence assays of mouse cells was performed directly in an eight-well microscopy chamber at room temperature. Cells were washed twice with PBS and fixed with 4% formaldehyde (Sigma; F8775) in PBS for 10 min. The cells were subsequently washed with PBS and permeabilized with 0.5% Triton X-100 (Roth; R30512) in PBS for 5 min, followed by another PBS wash. The permeabilized cells were blocked for 15 min in a blocking buffer (2% bovine serum albumin [Roth; 8076.2], 0.1% Triton X-100 in PBS), followed by a PBS wash.

Antibody labeling and immunofluorescence imaging

The primary antibody C3B9 (mouse monoclonal IgG2b; Woods *et al.*, 1989) was used for staining acetylated tubulin. The fixed *Leishmania* cells were incubated with C3B9 diluted 1:10 in PBS for 1 h in a humid chamber. The slides were then washed three times (5 min per wash) in PBS. Samples were incubated in TRITC-conjugated goat anti-mouse secondary antibody (115-025-146; Jackson ImmunoResearch Laboratories) (1:200 dilution in PBS plus 5% goat serum) for 1 h and again washed three times (5 min per wash) in PBS. Slides were mounted in 90% glycerol supplemented with 25 mg/ml 1,4-diazabicyclo[2.2.2]octane (DABCO) and 500 ng/µl diamidino-2-phenylindole (DAPI), pH 8.6, and imaged via fluorescence light microscopy as described above for live cell microscopy of *Leishmania*.

The fixed mouse cells were incubated with C3B9 diluted 1:50 in blocking buffer for 60 min. Next, the cells were thoroughly washed with PBS and stained for 30 min with Alexa Fluor 647–conjugated goat anti-mouse secondary antibody (A21235; Invitrogen) diluted 1:1000 in blocking buffer. Alternatively, the cells were stained with the primary antibody recognizing the ciliary protein Arl13b (17711-1; Proteintech), which was diluted 1:1000 in blocking buffer, followed by staining with Cy5-conjugated goat anti-rabbit (A10523; Invitrogen) secondary antibody diluted 1:1000 in blocking buffer. The labeled cells were subsequently washed with PBS and stained with 1 µg/ml DAPI in PBS for 5 min. Finally, the cells were washed with PBS, covered with 120 µl of 90% glycerol supplemented with DABCO, and stored at 4°C until imaging.

Mouse samples were imaged using a Leica TCS SP8 confocal microscope using an HC PL apochromatic × 63/1.40 oil objective. A fluorescent signal was detected using a combination of photomultiplier and hybrid detectors. Z-stacks were deconvolved with Huygens Professional v. 21.04 using deconvolution express mode (Scientific Volume Imaging, The Netherlands; http://svi.nl). Final three-dimensional (3D) visualization was rendered in Imaris viewer 9.7.2 (Bitplane). Selected confocal planes were processed using Fiji (Schindelin *et al.*, 2012).

Expansion microscopy

The specimen preparation was based on the U-ExM protocol (Gambarotto *et al.*, 2019) with a few modifications. Briefly, cells were fixed overnight in 4% formaldehyde and 4% acrylamide (Sigma; A8887) in PBS at room temperature. For gelation, the cells were incubated for 30 min at 37°C in a humidified incubator in 50 µl of monomer solution containing 19% sodium acrylate (Sigma; 408220), 10% acrylamide, 0.1% *N*,*N*′-methylenebisacrylamide (Sigma; M7256), 0.5% *N*,*N*,*N*′,*N*′-tetramethylethylenediamine (Sigma; T9281) and 0.5% ammonium persulfate (Thermo Scientific; 17874). After denaturation (60 min at 95°C in denaturation buffer composed of 50 mM Tris, 200 mM NaCl, and 200 mM SDS in ddH_2O; pH 9.0) and expansion of the gel by incubation in ultrapure water, a 1 × 1 cm piece of the gel was cut and incubated overnight with primary antibodies (C3B9; Woods *et al.*, 1989) diluted 1:10 and an anti-HA tag antibody (Cell Signaling Technology; 3724S) diluted 1:500 in 2% bovine serum albumin in PBS). After 3 × 20 min washes with ultrapure water, the gel was stained overnight with secondary antibodies (Alexa Fluor 488 anti-mouse [Invitrogen; A11001] diluted 1:500 and Alexa Fluor 555 anti-rabbit [Invitrogen; A21428] diluted 1:500 in 2% bovine serum albumin in PBS). Finally, the piece of gel was washed 3 × 20 min and stored in ultrapure water until imaging. The expanded gel was placed on a poly-L-lysine–coated glass-bottom dish (Cellvis; D35-20-1.5-N) and imaged as described above.

Transmission electron microscopy

Cells were prepared with a chemical fixation protocol similar to that outlined by Hoog *et al.* (2010). Briefly, cells were fixed with 2.5% glutaraldehyde and 4% paraformaldehyde in complete M199 culture medium for 2 h at room temperature. Fixed cells were washed six times for 10 min in 0.1 M piperazine-*N*,*N*′-bis(2-ethanesulfonic acid) buffer (PIPES, pH 7.2), with the fourth wash supplemented with 50 mM glycine. Cells were embedded in 3% low-melting-point agar and incubated in 1% osmium tetroxide and 1.5% potassium ferrocyanide in 0.1 M PIPES buffer rotating in darkness at 4°C for 1 h. Samples were then washed five times with ddH_2O (5 min per wash) and stained with 0.5% uranyl acetate at 4°C overnight in darkness. Samples were dehydrated, embedded in epoxy resin, sectioned, and stained as described previously (Hoog *et al.*, 2010). Electron micrographs were captured on a Tecnai 12 TEM (FEI) with an Ultrascan 1000 CCD camera (Gatan) and processed using Fiji (Schindelin *et al.*, 2012).

Biotin ligase-mediated proximity labeling

A cell line expressing LmxFused::BirA* was generated by tagging both *LmxFused* alleles with pPLOT-BirA*::3xmyc (Beneke *et al.*, 2017) and selected on 20 µg/ml puromycin. Clonal cell lines were selected by limiting dilution, and the modification of both alleles was confirmed via endpoint PCR (using primers that spanned the inserted BirA* tag encoding region; F: 5′-CGGGGCACTGAGCAACTTTGT-3′, R: 5′-CACCAGTGGGCAGTGTGAGC-3′). Biotinylated proteins were captured using the XL-BioID protocol, which includes a cross-linking step before affinity capture (Geoghegan *et al.*, 2022): Log-phase promastigote cultures (seeded at 2×10^6 cells/ml) were allowed to grow in complete M199 supplemented with 150 µM biotin (B-4639; Sigma-Aldrich) for 18–24 h. A total of 4×10^8 parasites were harvested via centrifugation (800 × *g* for 5 min), washed twice with PBS, and cross-linked with 1 mM dithiobis(succinimidyl propionate) (DSP) in 10 ml of PBS plus 5% dimethyl sulfoxide (DMSO) for 10 min at 28°C. Tris (1 M; pH 7.5) was added for 5 min at room temperature to quench, and parasites were pelleted via centrifugation (1200 × *g*, 3 min). All subsequent steps

were performed on ice or at 4°C. The supernatant was discarded and parasites lysed with sterile RIPA buffer plus protease and phosphatase inhibitors (1% NP-40, 0.5% sodium deoxycholate, 0.1% SDS, 50 mM Tris, pH 7.5, 125 mM NaCl, 0.1 mM EDTA, 0.1 mM phenylmethanesulfonyl fluoride [PMSF], 1 µg/ml pepstatin A, 1 µM trans-epoxysuccinyl-L-leucylamido(4-guanidino)butane [E-64], 0.4 mM 1–10 phenanthroline, 1 tablet/ml cOmplete protease inhibitor cocktail [Roche], 1× PhosSTOP [Roche], and 1× Halt protease inhibitors single-use cocktail [Thermo Scientific]) and sonicated (three times for 5 s at amplitude 16 on a MSE Soniprep 150). Benzonase (BaseMuncher; 0.5 U/µl) was added to digest chromatin for 1 h, and the lysate was centrifuged at 10,000 × *g* for 10 min at 4°C. The supernatant was added to 1 mg of MagResyn streptavidin beads (MR-STV002; Resyn Biosciences); note that these beads were washed twice with 1 ml of RIPA buffer before use and rotated overnight to enable biotinylated protein binding. The beads were then washed sequentially in 500 µl of RIPA buffer (four washes in total), followed by individual washes in 4 M urea, 6 M urea, and 1 M KCl. The beads were resuspended in 50 mM TEAB (triethylammonium bicarbonate). Samples capturing an equivalent fraction of the input material were collected at multiple points during the protocol, and SDS–PAGE and immunoblots were performed by standard methods using a mouse monoclonal anti-MYC antibody (clone 4A6; 05-724; Merck).

Mass spectrometry for BioID

Sample preparation and analysis was performed by the Advanced Proteomics Facility (Department of Biochemistry, University of Oxford) as follows: On-bead protein sample digests were performed according to the filter-aided sample preparation procedure described in Wisniewski *et al.* (2009). Peptides were analyzed by nano-liquid chromatography tandem mass spectrometry (nano-LC/MS/MS) on an Orbitrap Q Exactive mass spectrometer (Thermo Scientific) using higher-energy collisional dissociation (HCD) fragmentation. In brief, peptides were loaded on a C18 PepMap100 precolumn (300 µm i.d. × 5 mm; 100Å [Thermo Fisher Scientific]) at a flow rate of 12 µl/min in 100% buffer A (0.1% formic acid in H_20). Peptides were then transferred to an in-house-packed analytical column heated at 45°C (50 cm, 75 µm i.d. packed with ReproSil-Pur 120 C18-AQ, 1.9 µm, 120 Å) and separated using a 60 min gradient from 15 to 35% buffer B (0.1% formic acid in acetonitrile) at a flow rate of 200 nl/min. Q Exactive survey scans were acquired at 70,000 resolution to a scan range from 350 to 1500 m/z, automatic gain control target 3e6, maximum injection time 50 ms. The mass spectrometer was operated in a data-dependent mode to automatically switch between MS and MS/MS. The 10 most intense precursor ions were submitted to HCD fragmentation using an MS/MS resolution set to 17,500, a precursor automatic gain control target set to 5e4, a precursor isolation width set to 1.5 Da, and a maximum injection time set to 120 ms. The data were converted from .raw to .mgf file formats using ProteoWizard and analyzed through the Advanced Proteomics Facility Pipeline (CPFP; see Trudgian *et al.*, 2010). A list of proteins was generated using the CPFP meta-search Simple Protein Overview tool, using the *L. mexicana* proteome as reference (gene models based on Fiebig *et al.*, 2015) and label-free SINQ quantification, using search parameters outlined by Beneke *et al.* (2019). Proteins were filtered based on a 5% false discovery rate (FDR) and the identification of at least two unique peptides.

Immunoprecipitation

Cell lines expressing *LmxFused*::eYFP or *LmxULK4*::3xMYC were generated by tagging both alleles of the target gene with eYFP or 3xMYC, respectively, using the LeishGEdit method (Beneke *et al.*, 2017). Specific primers were designed for amplification of donor DNA cassettes, as follows. To tag the C-terminus of LmxULK4 with three MYC epitope tags, donor PCR products amplified from the standard pPLOT plasmids

F 5′-GAGGCGAACAAGATTCTGAAGAAACTCTCCGGATCCGGATCAGGATCTGG-3′

R 5′-AAATCGTACAGGCAACAGCAAACCCGCCCGCCAATTTGAGAGACCTGTGC-3′.

To generate donor PCR products for LmxFused C-terminal tagging with an eYFP tag without a MYC epitope, eYFP was amplified from the pJ1170/pLEnT-YB plasmid (Dean *et al.*, 2015):

F 5′-TACGTTGGCAACCTCGTCGATCGACTTGGTGGTTCTGGTAGTGGTTCCGGTTCCGGTTCTGTGAGCAAGGGCGAGGAGCTGTT-3′

R 5′-AAATCTGGAAAACGGCAACTATGAAGTCCGTTAGCCCTCCCACACATAACCAGAG-3′).

Immunoprecipitation with anti-GFP antibodies followed the protocol from Akiyoshi and Gull (2014), with the following modifications: Instead of using PEME buffer, cells were extracted directly in modified buffer H (BH)/0.15 (25 mM HEPES, pH 8.0, 2 mM $MgCl_2$, 0.1 mM EDTA, pH 8.0, 0.5 mM EGTA pH 8.0, 1% NP-40, 150 mM KCl, and 15% glycerol), including protease inhibitors (leupeptin, pepstatin, E-64, 20 µg/ml each, and 0.2 mM PMSF) and phosphatase inhibitors (1 mM sodium pyrophosphate, 2 mM Na-β-glycerophosphate, 0.1 mM Na_3VO_4, 5 mM NaF, and 100 nM microcystin-LR). Cell extracts were frozen in liquid N_2 and ground in a mortar and pestle, without sonication. Cell extracts were then centrifuged (14,000 × *g* for 30 min at 4°C), and only the supernatant was forwarded to IP. Post-IP bead samples were then washed twice in PBS and eluted in 0.2 M glycine, pH 2.5 (shaking at 21°C for 7 min), and neutralized with 10% volume 1 M Tris-HCl, pH 8.8. Equivalent proportions of each sample were collected at multiple points during the protocol, with SDS–PAGE and immunoblots performed by standard methods using the following mouse monoclonal antibodies: anti-GFP (11814460001; Roche) and anti-MYC (clone 4A6, 05-724; Merck).

LC-MS/MS for immunoprecipitation

Mass spectrometry analysis was performed by the Advanced Proteomics facility (Department of Biochemistry, University of Oxford). Peptides were separated by nano liquid chromatography (Thermo Scientific Ultimate RSLC 3000) coupled in line a Q Exactive mass spectrometer equipped with an Easy-Spray source (Thermo Fisher Scientific). Peptides were trapped onto a C18 PepMac100 precolumn (300 µm i.d. × 5 mm, 100Å; Thermo Fisher Scientific) using solvent A (0.1% formic acid, HPLC-grade water). The peptides were further separated onto an Easy-Spray RSLC C18 column (75 µm i.d., 50 cm length; Thermo Fisher Scientific) using a 60 min linear gradient (15 to 35% solvent B [0.1% formic acid in acetonitrile]) at a flow rate of 200 nl/min. The raw data were acquired on the mass spectrometer in a data-dependent acquisition mode (DDA). Full-scan MS spectra were acquired in the Orbitrap (scan range 350–1500 m/z, resolution 70,000; AGC target, 3e6, maximum injection time, 50 ms). The 10 most intense peaks were selected for higher-energy collision dissociation (HCD) fragmentation at 30% of normalized collision energy. HCD spectra were acquired in the Orbitrap at resolution 17,500, AGC target 5e4, maximum injection time 120 ms with fixed mass at 180 m/z. Charge exclusion was selected for unassigned and 1+ ions. The dynamic exclusion was set to 20 s.

Statistical analyses

Statistical analyses were performed on GraphPad Prism 9 software unless otherwise stated. The statistical tests employed here are outlined in the figure legends associated with each specific data set. Note that only directly comparable data sets were examined via multiple comparisons. Where appropriate, data sets were tested for normality using the D'Agostino and Pearson normality test (with normal QQ plots also visualized) to inform the selection of the parametric or nonparametric tests employed. Individual data points were plotted on all graphs as standard to provide transparency with respect to variance within and between the treatment groups/cell lines employed. Error bars were plotted as SD around the mean as standard.

ACKNOWLEDGMENTS

C.J.M. and E. G. were funded by the UK Medical Research Council (MRC) and the UK Department for International Development (DFID) under a MRC/DFID Concordat agreement; grant no. MR/R000859/1 (https://mrc.ukri.org/). E. G. was supported by a Royal Society University Research Fellowship (UF160661; https://royalsociety.org/).H.P-V. was supported by an ERASMUS+ mobility grant. T. B. was supported by a MRC PhD studentship (15/16_MSD_836338). The laboratory of V. V. was supported by Czech Science Foundation (GA CR) project no. 20-23165J and by an Installation Grant from the European Molecular Biology Organization. P.G. is a student of the Faculty of Science, Charles University, Prague, Czech Republic, which provided a PhD student fellowship. We acknowledge support for this project for E.G. through a WCIP core Wellcome Centre Award (104111/Z/14/Z) and through a Wellcome Trust grant (104627/Z/14/Z) to Keith Gull; https://wellcome.org). We acknowledge the Light Microscopy Core Facility, IMG CAS, Prague, Czech Republic, supported by MEYS (LM2018129, CZ.02.1.01/0.0/0.0/18_046/0016045) and RVO: 68378050-KAV-NPUI for their support with the confocal imaging of ependymal cells. The funders had no role in study design, data collection and analysis, decision to publish, or preparation of the manuscript. We thank Sabrina Liberatori and Marjorie Fournier (University of Oxford Proteomics facility) for mass spectrometry support, Raman Dhaliwal and Errin Johnson (Dunn School Bioimaging facility) for electron microscopy support, James Smith (University of Oxford) for help with the generation of Leishmania mutants, Richard Wheeler (University of Oxford) for advice on IFT measurements, Bungo Akiyoshi (University of Oxford) for advice on the IP protocol, Alice Meunier and Nathalie Spassky (ENS Paris) for introducing us to preparation of ependymal cell cultures, Jeremy Mottram and Vincent Geoghegan (University of York) for sharing their XL-BioID protocol before publication, and Keith Gull (University of Oxford) for antibody C3B9, access to laboratory equipment. and helpful comments on the manuscript.

REFERENCES

Akiyoshi B, Gull K (2014). Discovery of unconventional kinetochores in kinetoplastids. Cell 156, 1247–1258.

Amos B, Aurrecoechea C, Barba M, Barreto A, Basenko EY, Bazant W, Belnap R, Blevins AS, Bohme U, Brestelli J, *et al.* (2021). VEuPathDB: the eukaryotic pathogen, vector and host bioinformatics resource center. Nucleic AcidsRes 50, D898–D911.

Baker N, Catta-Preta CMC, Neish R, Sadlova J, Powell B, Alves-Ferreira EVC, Geoghegan V, Carnielli JBT, Newling K, Hughes C, *et al.* (2022). Systematic functional analysis of *Leishmania* protein kinases identifies regulators of differentiation or survival. Nat Commun 12, 1244.

Beneke T, Demay F, Hookway E, Ashman N, Jeffery H, Smith J, Valli J, Becvar T, Myskova J, Lestinova T, *et al.* (2019). Genetic dissection of a *Leishmania* flagellar proteome demonstrates requirement for directional motility in sand fly infections. PLoS Pathog 15, e1007828.

Beneke T, Gluenz E (2019). LeishGEdit: A Method for Rapid Gene Knockout and Tagging Using CRISPR-Cas9. Methods Mol Biol 1971, 189–210.

Beneke T, Madden R, Makin L, Valli J, Sunter J, Gluenz E (2017). A CRISPR Cas9 high-throughput genome editing toolkit for kinetoplastids. R Soc Open Sci 4, 170095.

Chen MH, Gao N, Kawakami T, Chuang PT (2005). Mice deficient in the fused homolog do not exhibit phenotypes indicative of perturbed hedgehog signaling during embryonic development. Mol Cell Biol 25, 7042–7053.

Dean S, Sunter J, Wheeler R \J, Hodkinson I, Gluenz E, Gull K (2015). A toolkit enabling efficient, scalable and reproducible gene tagging in trypanosomatids. Open Biol 5, 140197.

Delgehyr N, Meunier A, Faucourt M, Bosch Grau M, Strehl L, Janke C, Spassky N (2015). Ependymal cell differentiation, from monociliated to multiciliated cells. Methods Cell Biol 127, 19– 35.

Edelbusch C, Cindric S, Dougherty GW, Loges NT, Olbrich H, Rivlin J, Wallmeier J, Pennekamp P, Amirav I, Omran H (2017). Mutation of serine/threonine protein kinase 36 (STK36) causes primary ciliary dyskinesia with a central pair defect. Hum Mutat 38, 964–969.

Fiebig M, Kelly S, Gluenz E (2015). Comparative lifecycle transcriptomics revises *Leishmania mexicana* genome annotation and links a chromosome duplication with parasitism of vertebrates. PLoS Pathog 11, e1005186.

Gambarotto D, Zwettler FU, Le Guennec M, Schmidt-Cernohorska M, Fortun D, Borgers S, Heine J, Schloetel JG, Reuss M, Unser M, *et al.* (2019). Imaging cellular ultrastructures using expansion microscopy (U-ExM). Nat Methods 16, 71–74.

Geoghegan V, Carnielli JBT, Jones NG, Saldivia M, Antoniou S, Hughes C, Neish R, Dowle A, Mottram JC (2022). CLK1/CLK2-driven signalling at the Leishmania kinetochore is captured by spatially referenced proximity phosphoproteomics. Commun Biol 5, 1305.

Goetz SC, Anderson KV (2010). The primary cilium: a signalling centre during vertebrate development. Nat Rev Genet 11, 331–344.

Hoog JL, Gluenz E, Vaughan S, Gull K (2010). Ultrastructural investigation methods for *Trypanosoma brucei*. Methods Cell Biol 96, 175–196.

Janke C, Montagnac G (2017). Causes and consequences of microtubule acetylation. Curr Biol 27, R1287–R1292.

Jones NG, Thomas EB, Brown E, Dickens NJ, Hammarton TC, Mottram JC (2014). Regulators of *Trypanosoma brucei* cell cycle progression and differentiation identified using a kinome-wide RNAi screen. PLoS Pathog 10, e1003886.

Khalifa AAZ, Ichikawa M, Dai D, Kubo S, Black CS, Peri K, McAlear TS, Veyron S, Yang SK, Vargas J, *et al.* (2020). The inner junction complex of the cilia is an interaction hub that involves tubulin post-translational modifications. eLife 9, e52760.

Kumar S, Stecher G, Tamura K (2016). MEGA7: Molecular Evolutionary Genetics Analysis Version 7.0 for Bigger Datasets. Mol Biol Evol 33, 1870–1874.

Lang B, Zhang L, Jiang G, Hu L, Lan W, Zhao L, Hunter I, Pruski M, Song NN, Huang Y, *et al.* (2016). Control of cortex development by ULK4, a rare risk gene for mental disorders including schizophrenia. Sci Rep 6, 31126.

Lechtreck KF (2015). IFT-cargo interactions and protein transport in cilia. Trends Biochem Sci 40, 765–778.

Lee L (2011). Mechanisms of mammalian ciliary motility: insights from primary ciliary dyskinesia genetics. Gene 473, 57–66.

Li H, Durbin R (2009). Fast and accurate short read alignment with Burrows-Wheeler transform. Bioinformatics 25, 1754–1760.

Li H, Handsaker B, Wysoker A, Fennell T, Ruan J, Homer N, Marth G, Abecasis G, Durbin R, 1000 Genome Project Data Processing Subgroup (2009). The Sequence Alignment/Map format and SAMtools. Bioinformatics 25, 2078–2079.

Liu M, Guan Z, Shen Q, Lalor P, Fitzgerald U, O'Brien T, Dockery P, Shen S (2016). Ulk4 is essential for ciliogenesis and CSF flow. J Neurosci 36, 7589–7600.

Ma M, Stoyanova M, Rademacher G, Dutcher SK, Brown A, Zhang R (2019). Structure of the decorated ciliary doublet microtubule. Cell 179, 909–922.e912.

Maloverjan A, Piirsoo M (2012). Mammalian homologues of Drosophila fused kinase. Vitam Horm 88, 91–113.

Maloverjan A, Piirsoo M, Kasak L, Peil L, Osterlund T, Kogerman P (2010). Dual function of UNC-51-like kinase 3 (Ulk3) in the Sonic hedgehog signaling pathway. J Biol Chem 285, 30079–30090.

Mangeol P, Prevo B, Peterman EJ (2016). KymographClear and KymographDirect: two tools for the automated quantitative analysis of molecular and cellular dynamics using kymographs. Mol Biol Cell 27, 1948–1957.

Merchant M, Evangelista M, Luoh SM, Frantz GD, Chalasani S, Carano RA, van Hoy M, Ramirez J, Ogasawara AK, McFarland LM, *et al*. (2005). Loss of the serine/threonine kinase fused results in postnatal growth defects and lethality due to progressive hydrocephalus. Mol Cell Biol 25, 7054–7068.
Moreira-Leite FF, Sherwin T, Kohl L, Gull K (2001). A trypanosome structure involved in transmitting cytoplasmic information during cell division. Science 294, 610–612.
Murone M, Luoh SM, Stone D, Li W, Gurney A, Armanini M, Grey C, Rosenthal A, de Sauvage FJ (2000). Gli regulation by the opposing activities of fused and suppressor of fused. Nat Cell Biol 2, 310–312.
Nakayama K, Katoh Y (2018). Ciliary protein trafficking mediated by IFT and BBSome complexes with the aid of kinesin-2 and dynein-2 motors. J Biochem 163, 155–164.
Nozawa YI, Yao E, Gacayan R, Xu SM, Chuang PT (2014). Mammalian Fused is essential for sperm head shaping and periaxonemal structure formation during spermatogenesis. Dev Biol 388, 170–180.
Nozawa YI, Yao E, Lin C, Yang JH, Wilson CW, Gacayan R, Chuang PT (2013). Fused (Stk36) is a ciliary protein required for central pair assembly and motile cilia orientation in the mammalian oviduct. Dev Dyn 242, 1307–1319.
Owa M, Uchihashi T, Yanagisawa HA, Yamano T, Iguchi H, Fukuzawa H, Wakabayashi KI, Ando T, Kikkawa M (2019). Inner lumen proteins stabilize doublet microtubules in cilia and flagella. Nat Commun 10, 1143.
Portran D, Schaedel L, Xu Z, Thery M, Nachury MV (2017). Tubulin acetylation protects long-lived microtubules against mechanical ageing. Nat Cell Biol 19, 391–398.
Preat T, Therond P, Lamour-Isnard C, Limbourg-Bouchon B, Tricoire H, Erk I, Mariol MC, Busson D (1990). A putative serine/threonine protein kinase encoded by the segment-polarity fused gene of Drosophila. Nature 347, 87–89.
Preuss F, Chatterjee D, Mathea S, Shrestha S, St-Germain J, Saha M, Kannan N, Raught B, Rottapel R, Knapp S (2020). Nucleotide binding, evolutionary insights, and interaction partners of the pseudokinase Unc-51-like kinase 4. Structure 28, 1184–1196.e1186.
Ringers C, Olstad EW, Jurisch-Yaksi N (2020). The role of motile cilia in the development and physiology of the nervous system. Philos Trans R Soc Lond, B, Biol Sci 375, 20190156.
Robinson JT, Thorvaldsdottir H, Winckler W, Guttman M, Lander ES, Getz G, Mesirov JP (2011). Integrative genomics viewer. Nat Biotechnol 29, 24–26.
Romano V, de Beer TA, Schwede T (2017). A computational protocol to evaluate the effects of protein mutants in the kinase gatekeeper position on the binding of ATP substrate analogues. BMC Res Notes 10, 104.
Roux KJ, Kim DI, Raida M, Burke B (2012). A promiscuous biotin ligase fusion protein identifies proximal and interacting proteins in mammalian cells. J Cell Biol 196, 801–810.
Schindelin J, Arganda-Carreras I, Frise E, Kaynig V, Longair M, Pietzsch T, Preibisch S, Rueden C, Saalfeld S, Schmid B, *et al*. (2012). Fiji: an open-source platform for biological-image analysis. Nat Methods 9, 676–682.
Shaner NC, Lambert GG, Chammas A, Ni Y, Cranfill PJ, Baird MA, Sell BR, Allen JR, Day RN, Israelsson M, *et al*. (2013). A bright monomeric green fluorescent protein derived from Branchiostoma lanceolatum. Nat Methods 10, 407–409.
Shaw AS, Kornev AP, Hu J, Ahuja LG, Taylor SS (2014). Kinases and pseudokinases: lessons from RAF. Mol Cell Biol 34, 1538–1546.
Shi Q, Li S, Jia J, Jiang J (2011). The Hedgehog-induced Smoothened conformational switch assembles a signaling complex that activates Fused by promoting its dimerization and phosphorylation. Development 138, 4219–4231.
Smertenko A, Hewitt SL, Jacques CN, Kacprzyk R, Liu Y, Marcec MJ, Moyo L, Ogden A, Oung HM, Schmidt S, *et al*. (2018). Phragmoplast microtubule dynamics—a game of zones. J Cell Sci 131, jcs203331.
Stoddard D, Zhao Y, Bayless BA, Gui L, Louka P, Dave D, Suryawanshi S, Tomasi RF, Dupuis-Williams P, Baroud CN, *et al*. (2018). *Tetrahymena* RIB72A and RIB72B are microtubule inner proteins in the ciliary doublet microtubules. Mol Biol Cell 29, 2566–2577.
Tang L, Franca-Koh J, Xiong Y, Chen MY, Long Y, Bickford RM, Knecht DA, Iglesias PA, Devreotes PN (2008). tsunami, the *Dictyostelium* homolog of the Fused kinase, is required for polarization and chemotaxis. Genes Dev 22, 2278–2290.
Tapia Contreras C, Hoyer-Fender S (2020). The WD40-protein CFAP52/WDR16 is a centrosome/basal body protein and localizes to the manchette and the flagellum in male germ cells. Sci Rep 10, 14240.
Ta-Shma A, Perles Z, Yaacov B, Werner M, Frumkin A, Rein AJ, Elpeleg O (2015). A human laterality disorder associated with a homozygous WDR16 deletion. Eur J Hum Genet 23, 1262–1265.
Tillberg PW, Chen F, Piatkevich KD, Zhao Y, Yu CC, English BP, Gao L, Martorell A, Suk HJ, Yoshida F, *et al*. (2016). Protein-retention expansion microscopy of cells and tissues labeled using standard fluorescent proteins and antibodies. Nat Biotechnol 34, 987–992.
Trudgian DC, Ridlova G, Fischer R, Mackeen MM, Ternette N, Acuto O, Kessler BM, Thomas B (2011). Comparative evaluation of label-free SINQ normalized spectral index quantitation in the central proteomics facilities pipeline. Proteomics 11, 2790–2797.
Trudgian DC, Thomas B, McGowan SJ, Kessler BM, Salek M, Acuto O (2010). CPFP: a central proteomics facilities pipeline. Bioinformatics 26, 1131–1132.
UniProt Consortium (2021). UniProt: the universal protein knowledgebase in 2021. Nucleic Acids Res 49, D480–D489.
Varga V, Moreira-Leite F, Portman N, Gull K (2017). Protein diversity in discrete structures at the distal tip of the trypanosome flagellum. Proc Natl Acad Sci USA 114, E6546–E6555.
Vogel P, Read RW, Hansen GM, Payne BJ, Small D, Sands AT, Zambrowicz BP (2012). Congenital hydrocephalus in genetically engineered mice. Vet Pathol 49, 166–181.
Wheeler RJ (2017). Use of chiral cell shape to ensure highly directional swimming in trypanosomes. PLoS Comput Biol 13, e1005353.
Wheeler RJ, Gluenz E, Gull K (2015). Routes to a 9+0 flagellum: Basal body multipotency and axonemal plasticity. Nature Commun 6, 8964.
Wheeler RJ, Sunter JD, Gull K (2016). Flagellar pocket restructuring through the *Leishmania* life cycle involves a discrete flagellum attachment zone. J Cell Sci 129, 854–867.
Wilson CW, Nguyen CT, Chen MH, Yang JH, Gacayan R, Huang J, Chen JN, Chuang PT (2009). Fused has evolved divergent roles in vertebrate Hedgehog signalling and motile ciliogenesis. Nature 459, 98–102.
Wisniewski JR, Zougman A, Nagaraj N, Mann M (2009). Universal sample preparation method for proteome analysis. Nat Methods 6, 359–362.
Woods A, Sherwin T, Sasse R, MacRae TH, Baines AJ, Gull K (1989). Definition of individual components within the cytoskeleton of *Trypanosoma brucei* by a library of monoclonal antibodies. J Cell Sci 93 (Pt 3), 491–500.
Zhang Y, Mao F, Lu Y, Wu W, Zhang L, Zhao Y (2011). Transduction of the Hedgehog signal through the dimerization of Fused and the nuclear translocation of Cubitus interruptus. Cell Res 21, 1436–1451.
Zhou Q, An T, Pham KTM, Hu H, Li Z (2018). The CIF1 protein is a master orchestrator of trypanosome cytokinesis that recruits several cytokinesis regulators to the cytokinesis initiation site. J Biol Chem 293, 16177–16192.